Effects of a thermal perturbation on mineralogy and pore water composition in a clay-rock: an experimental and modeling study

Hélène Gailhanou, Catherine Lerouge, Mathieu Debure, Stéphane Gaboreau, Eric C. Gaucher, Sylvain Grangeon, Jean-Marc Greneche, M. Kars, Benoit Madé, Nicolas C.M. Marty, et al.

Available online at www.sciencedirect.com

ScienceDirect

Geochimica et Cosmochimica Acta 197 (2017) 193–214

Geochimica et Cosmochimica Acta

www.elsevier.com/locate/gca

Effects of a thermal perturbation on mineralogy and pore water composition in a clay-rock: An experimental and modeling study

H. Gailhanou [a,*], C. Lerouge [a], M. Debure [a], S. Gaboreau [a], E.C. Gaucher [a], S. Grangeon [a], J.-M. Grenèche [b], M. Kars [c], B. Madé [d], N.C.M. Marty [a], F. Warmont [e], C. Tournassat [f,*]

[a] *BRGM – Water, Environment and Ecotechnology Division, 3 Av. Claude Guillemin, 45060 Orléans cedex 2, France*
[b] *Institut des Molécules et Matériaux du Mans, UMR CNRS 6283, Université du Maine, 72085 Le Mans cedex, France*
[c] *Center for Advanced Marine Core Research, Kochi University, B200 Monobe, Nankoku 783-8502, Japan*
[d] *Andra – Parc de la Croix Blanche, 1-7 rue Jean Monnet, 92298 Châtenay-Malabry Cedex, France*
[e] *ICMN, CRMD-CNRS, 1b Rue de la Ferollerie, 45071 Orléans, France*
[f] *Université d'Orléans – CNRS/INSU – BRGM, UMR 7327 Institut des Sciences de la Terre d'Orléans, 45071 Orléans, France*

Received 8 June 2016; revised 7 October 2016; accepted in revised form 13 October 2016; available online 19 October 2016

Abstract

The physical and chemical properties of clay-rocks are, at least partly, controlled by the chemical composition of their pore water. In evaluating the concept of disposing of radioactive waste in clay-rock formations, determining pore water composition is an important step in predicting how a clay-rock will behave over time and as a function of external forces, such as chemical and thermal perturbations. This study aimed to assess experimental and modeling methodology to calculate pore water composition in a clay-rock as a function of temperature (up to 80 °C). Hydrothermal alteration experiments were carried out on clay-rock samples. We conducted comprehensive chemical and mineralogical characterization of the material before and after reaction, and monitored how the chemical parameters in the liquid and gas phases changed. We compared the experimental results with the *a priori* predictions made by various models that differed in their hypotheses on the reactivity of the minerals present in the system. Thermodynamic equilibrium could not be assessed unequivocally in these experiments and most of the predicted mineralogy changes were too subtle to be tracked quantitatively. However, from observing the neoformation of minerals such as goethite we were able to assess the prominent role of Fe-bearing phases in the outcome of the experiments, especially for the measured pH and p_{CO2} values. After calibrating the amount of reacting Fe-bearing phases with our data, we proposed a thermodynamic model that was capable of predicting the chemical evolution of the systems under investigation as well as the evolution of other systems already published in the literature, with the same clay-rock material but with significant differences in experimental conditions.

Keywords: Clay; Radioactive waste storage; Pore water; Modeling; Thermodynamics; Hydrothermal alteration

* Corresponding authors.
E-mail addresses: h.gailhanou@brgm.fr (H. Gailhanou), c.tournassat@brgm.fr (C. Tournassat).

http://dx.doi.org/10.1016/j.gca.2016.10.004
0016-7037/

1. INTRODUCTION

The effectiveness of radioactive waste disposal in clay-rock formations relies in large part on how the host-rocks restrict radionuclide mass transport diffusion processes, on how they reduce dissolved radionuclide concentrations in the pore water by adsorption and precipitation phenomena, and on how favorable their mechanical properties are, for instance whether they allow fracture self-sealing in zones damaged by excavation procedures (Landais, 2006; Delay et al., 2007; Neuzil, 2013; Bianchi et al., 2014). The physical and chemical properties of clay-rocks are, at least partly, controlled by the chemical composition of their pore water, so assessing the stability of the physical and chemical properties of the host-rocks over geological time periods is of paramount importance. Determining pore water composition is an important step in predicting how a clay-rock will behave over time as a function of external forcing (Rosenqvist, 1984; Moore, 1991; Savage et al., 2002; Gaucher and Blanc, 2006; Altmann, 2008; Marty et al., 2009, 2014; Gaboreau et al., 2012; Zachara et al., 2016). Pore waters are however notoriously difficult to sample directly from clay-rocks, and sampling methods can result in many artifacts that impact the measured concentrations (Fernández et al., 2014; Mazurek et al., 2015). To circumvent this problem, a range of experimental and modeling methods have been developed or improved in the last two decades to characterize the chemical composition of pristine pore water. A comprehensive review of these methods and their associated commonly encountered errors and difficulties can be found in Tournassat et al. (2015). The overall consistency between measured chemical compositions, compositions that can be predicted from thermodynamic models, and information obtained from the solid (at least cation exchange composition, mineralogical composition and isotopic composition), is commonly taken as the basis for how much confidence we can put in the pore water composition determination.

Among the range of perturbations that are foreseen in a radioactive waste repository, thermal perturbations cannot be avoided because of the heat generated by the radioactive decay of the radioelements in the waste canisters. In the near-field of high-level radioactive waste storage, a temperature increase of up to 80–120 °C is expected, depending on the storage concept and size (Andra, 2005). So understanding and predicting the effect of the thermal perturbation on pore water composition is a key aspect of modeling the long-term evolution of radioactive waste disposals. For systems under perturbation, the question of the reliability of pore water composition determination is even more problematic than for pristine systems. In most cases, samples that are fully representative of the conditions of interest and from which pore water could be extracted and analyzed are missing. The time that would be necessary to achieve full equilibrium between the solid phases and the pore water, and the absence of clear criteria that could be used to state that full equilibrium has been achieved, could be a problem that is difficult to overcome. Consequently, determining the composition of perturbed pore water inevitably relies for a large part on predictive modeling efforts. In undisturbed systems, pore water models are based on the Gibbs' phase rule that takes advantage of the hypothesis of local equilibrium between the pore water composition and surrounding reacting mineral phases (Bradbury and Baeyens, 1998; Beaucaire et al., 2000, 2008, 2012; Motellier et al., 2003; Pearson et al., 2003, 2011; Gaucher et al., 2006, 2009; Tremosa et al., 2012; Tournassat et al., 2015). The underlying justifications of this strong hypothesis are (i) that diffusion processes drive exchanges between the pore water in clay-rocks and the surrounding environment, (ii) that the mineral grains in clay-rocks are usually small, so they have a high specific surface area (SSA) that increases dissolution/precipitation kinetics, and (iii) that the interaction time has been long enough to establish equilibrium conditions between the pore water and a pool of minerals that includes minerals with low kinetic rates of dissolution or precipitation. In systems under perturbation, the third point is far from being certain, depending on the duration of the perturbation. In addition, while it is quite straightforward to choose the nature of the phases that must be considered in the Gibb's phase rule for a pristine system – it must be the phases that are observed in the sample and that show some indications of having reached equilibrium (Gaucher et al., 2006; Lerouge et al., 2011; Kars et al., 2015) – choosing is far more problematic for a system under perturbation, for which, if a sample is made available, it is more difficult to assess equilibrium criteria. Most often, the pore water composition prediction depends on (i) guesses by modelers for the choice of phases that may or may not, or are likely or unlikely to appear during the perturbation, (ii) the related completeness of the thermodynamic database that is used to make this choice, and (iii) the accuracy of the thermodynamic values that are tabulated as a function of temperature. In addition, dissolution/precipitation kinetic considerations and the underlying hypotheses on reactive surface area and kinetic rates can also interfere with the final result.

The goal of our study was to tackle the problem of how to predict pore water composition as a function of temperature using a stepwise approach combining modeling and experiments carried out on clay-rock samples that are representative of expected geological storage sites. In a first step, a set of pore water compositions were calculated at 80 °C (i) by using a modified version of a model previously published for predicting composition at 25 °C (Gaucher et al., 2009) and (ii) by applying a set of hypotheses made on the reactivity of mineral phases at 80 °C. We then chose a reference composition at 80 °C, and designed long-term solid–solution equilibration experiments accordingly to check the validity of the modeling predictions. In a final step, a comparison was made between the pore water composition predictions (and their underlying assumptions) and the actual solution and solid phase compositions that were determined before, during and after the experiments. This manuscript is organized with that stepwise approach in mind.

2. MATERIALS AND METHODS

2.1. Preliminary predictive modeling of pore water composition at 80 °C

2.1.1. Basic principles for pore water composition modeling

The pore water equilibrium model from Gaucher et al. (2009) and the resulting pore water composition at 25 °C were taken as the starting points for the predictive model at 80 °C. In the following paragraphs we provide a short summary of the approach. More details can be found in the literature (Gaucher et al., 2009; Pearson et al., 2011; Tournassat et al., 2015). As already stated in the introduction, pore water models are based on the Gibbs' phase rule:

$$F = C - P + 2 \quad (1)$$

where F is the variance or the number of degrees of freedom of the system, C is the number of independent components, and P is the number of phases in equilibrium with each other; the extra 2 is related to the pressure and temperature parameters. The objective of pore water composition models is to reduce the number of degrees of freedom to zero. At fixed temperature and pressure, this objective is met for $P = C$, i.e. the number of phases must equal the number of components to obtain the pore water composition. Some constituents such as Cl^- or Br^- are not controlled by the solubility of any phases in the system. They are called "free components" in the following and their concentration must be fixed. Because some elements have solute species that can be found simultaneously in various redox states (Fe, S), the redox potential of the pore water must also be constrained, thus adding one degree of freedom to the system. As a rule, to predict the pore water concentrations of n elements including their redox speciation, we need to find $n + 1$ independent phases/reactions (not considering the free components). The aqueous phase itself must be considered in the number of independent phases (in practice it adds a numerical constraint to the electro-neutrality). Considering mineral dissolution/precipitation and cation exchange reactions provides the necessary additional constraints for the system. Cation exchange reactions, which are often included in pore water modeling (Bradbury and Baeyens, 1998; Pearson et al., 2003, 2011; Gaucher et al., 2006, 2009; Beaucaire et al., 2012; Tremosa et al., 2012; Tournassat et al., 2015), cannot really be considered as a phase in the sense of the Gibbs' phase rule, but considering them helps to reduce the number of independent components C in Eq. (1) (for more details, see Tournassat et al. (2015)). As an illustration, the model used to obtain the chemical composition of the pore water at 25 °C in the Callovian-Oxfordian clay-rock at Bure (France) from Gaucher et al. (2009) is summarized in Fig. 1, and its result is compared to a seepage water composition that is considered to be representative of the pore water composition (Vinsot et al., 2008).

2.1.2. Working hypothesis for calculations at 80 °C

The predictive modeling of the chemical composition of pore water as a function of temperature followed three important assumptions. The first was that local equilibrium between the rock components and the pore water composition can be attained during the thermal perturbation. The second was that the concentrations of free components (Cl^-, Br^-), which are not involved in chemical reactions, do not change with temperature, and so remain at the same value as at 25 °C (i.e. the *in situ* desaturation–re-saturation

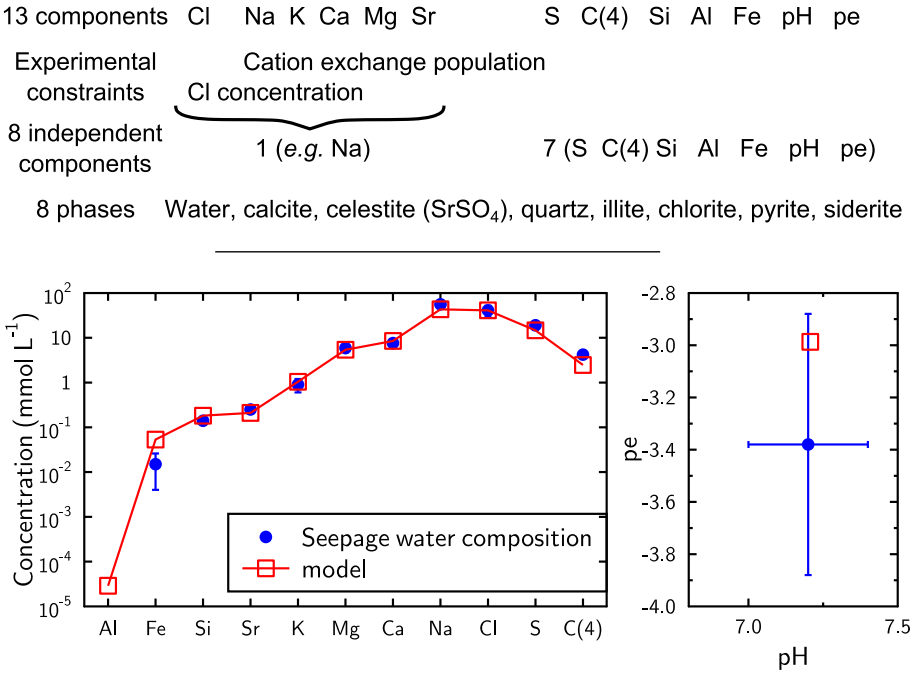

Fig. 1. Top: the fully constrained pore water model for the system pH, pe, Cl, S, Na, K, Ca, Mg, Sr, C(4), Si, Al, Fe in the Callovian-Oxfordian clay-rock (Bure, France) at 25 °C. Bottom: corresponding predicted pore water composition as compared to seepage water composition. Reproduced from Tournassat et al. (2015).

phenomenology following temperature increase is neglected in the proposed model). The third, which may be connected to the second, is that the *in situ* solid to liquid ratio does not change with temperature, meaning that the *in situ* water content of the rock remains at ~0.08 $kg_{water}\ kg^{-1}_{wet\ rock}$. This last assumption is important, because cation exchange reactions are involved in the equilibria between the pore water composition and the solid phase, so cation redistribution between the exchanger and the water can lead to the precipitation of secondary mineral phases without the complete dissolution of a phase from the initial mineral assemblage. How cations are redistributed between the solution and the exchanger with temperature depends on the concentration of cation exchange sites in the system, which is given by the cation exchange capacity (CEC) multiplied by the *in situ* solid to liquid ratio. Consequently, we had also to consider that the CEC does not change with temperature. This last hypothesis must be checked by verifying that the predicted content and nature of the clay minerals in the system modeled at 80 °C is not significantly different from those in the system at 25 °C.

2.1.3. Model scenarios

Two modeling scenarios were tested to estimate *a priori* the pore water composition in the Callovian-Oxfordian clay-rock at 80 °C. Both scenarios were based on the chlorite-Cca-2/illite-Imt-2 model from Gaucher et al. (2009). In the first scenario, only fast reacting mineral phases were considered in the model (carbonate and sulfate minerals). In particular, here we excluded clay minerals because of their low dissolution kinetic rate at near neutral pH (Cama et al., 2000; Rozalén et al., 2008, 2009; Marty et al., 2011, 2015). This first model aimed at mimicking the fast change in pore water chemistry in the presence of a temperature increase in a short-term laboratory experiment. The second modeling scenario took into account the whole mineral assemblage. In both scenarios, cation exchange reactions were taken into account. The cation exchange selectivity coefficient values at 80 °C were unfortunately not available. In a first approach, we used pragmatically their corresponding values at 25 °C in agreement with the practice of other authors (Beaucaire et al., 2012). The Thermochimie database (Giffaut et al., 2014) was used to perform the calculations. For comparison, the Thermoddem database (Blanc et al., 2012) was also used. These two databases differ mostly in the numerical method used to account for the temperature effect in calculating solute speciation and phase solubility: the van't Hoff equation in Thermochimie versus a polynomial expression in Thermoddem. These two databases are available online (https://www.thermochimie-tdb.com/; http://thermoddem.brgm.fr/). All calculations were carried out with PHREEQC version 3 (Parkhurst and Appelo, 1999, 2013).

2.2. Experimental setup and materials

2.2.1. Callovian-Oxfordian rock samples

The core sample EST26479 used for the hydrothermal experiments was collected in May 2007 at a depth of −124.06 m (Z_{NGF}; NGF: Nivellement Général de la France), corresponding to the C2b1 unit of the Callovian-Oxfordian Formation (Gaucher et al., 2004). The sample was obtained from the FOR1118 horizontal 8 cm diameter borehole that was drilled under N_2 flux at a distance of 13.7 m from the tunnel in the Andra underground research laboratory (URL) at Bure (France) (Claret et al., 2010; Kars et al., 2015). The sample was conditioned under nitrogen gas in a stainless steel container tight to the gases immediately after drilling. It was then transferred into a glove box and kept preserved from O_2 in a nitrogen atmosphere (O_2 concentration lower than or equal to 1 ppm). Prior to the experiment, the sample was crushed by hand at a fraction size <80 μm in a glove box under nitrogen atmosphere. The rim of the core was discarded (~1 cm) before crushing because of its possible contamination by O_2 during handling just after drilling. In what follows, this sample is called "clay-rock sample". It was then transferred into a glove box and kept preserved from O_2 in a nitrogen atmosphere (O_2 concentration lower than or equal to 1 ppm). The hydrothermal alteration experiments started in 2008 and ended in 2013.

The clay fraction (<2 μm) of another core sample from the C2b1 unit (sample K119) was used for cation-exchange experiments. The sample preparation was described in Tournassat et al. (2009) and included <2 μm separation by centrifugation and removal of carbonate minerals and organic matter by chemical treatments. In what follows, this sample is called "clay fraction".

2.2.2. Chemicals

All solutions and suspensions were prepared with Millipore Milli-Q 18 MΩ·cm water. The synthetic solutions described below (using $CaSO_4{:}2H_2O$, $MgSO_4{:}7H_2O$, KCl, NaCl, $SrCl_2{:}6H_2O$, Na_2SO_4 and $NaHCO_3$ salts) and the NaCl, KCl, $MgCl_2$, $SrCl_2$, and $CaCl_2$ solutions for cation exchange experiments were prepared from analytical grade salts.

2.2.3. Analytical methods

Partial pressures of CO_2, O_2, CH_4 and H_2S were determined using gas chromatography (CPG type VARIAN 3400, quantification limit 0.001 vol.%). Cations (Ca^{2+}, Mg^{2+}, Na^+, K^+, Sr^{2+}, NH_4^+, total Al and total Fe) and silica concentrations in solution were determined by inductively coupled plasma-atomic emission spectroscopy (ICP-AES, Jobin Yvon) or by mass spectroscopy (ICP-MS, Thermo Fisher Scientific). Fe^{2+} concentrations were determined by colorimetry, by using phenanthroline as Fe^{2+} complex agent in the presence of acetate pH buffer. Chloride and sulfate anions concentration were measured by ion chromatography (HPLC, Dionex). Dissolved inorganic carbon (DIC) concentrations were determined using IR spectroscopy (TOC Analyzer, Shimadzu). Before analysis, all the solutions were filtered at 0.1 μm (Millipore Millex-VV, PVDF).

2.2.4. Berghof reactors and Parr pressure vessel

The water–gas–clay–rock equilibrium experiments at 80 °C were carried out in 350 mL stainless-steel Berghof

BR300 reactors. The reactors were equipped with a pressure gauge (0–10 bars with 0.1 % accuracy) and several gas and liquid sampling valves. To prevent chemical interactions between the steel container and the clay dispersion during the experiments, the tank of the reactor contained a PTFE insert. The reactor was surrounded by a heater, equipped with a thermal regulation system to maintain the temperature inside the reactor at 80 °C (±2 °C). The pressure inside the reactor was monitored continuously, in particular to check for the absence of leakage.

A pressure vessel from Parr Instrument, was also used. It was made of titanium, with a volume of 45 mL, and equipped with a gas sampling valve. The single rigid gasket was made of PTFE. The absence of water evaporation (and thus leakage) was checked by periodic weighing at 80 °C during the experiment. In this experiment, the clay-rock suspension was in direct contact with the titanium metal.

2.2.5. Experimental method for hydrothermal experiments at 80 °C

For all of the experiments the solid to liquid ratio was set to ~100 g·L^{-1}. The exact experimental conditions are summarized in Table 1.

The hydrothermal experiments had two main stages: (i) preparing a mixture between a synthetic solution and the clay-rock sample at room temperature 21 °C ± 1 °C under anoxic atmosphere, and (ii) closing the reactor and heating at 80 °C. The composition of the synthetic solution approximately matched the composition given by the preliminary predictive calculations (see above), except for pH and thus partial pressure of CO_2 that were initially adjusted to be close to those expected at equilibrium in the water-clay-rock system at 25 °C. The synthetic solution used for the experiments was prepared initially at room temperature in a glove box under nitrogen atmosphere ([O_2] < 1 ppm). This preparation method required particular precautions to limit the outgassing of the solution that would have caused significant disturbances in pH, DIC and p_{CO2} values.

A first method (Method 1) of preparation of the synthetic solution was applied to experiments 1 and 2. It was a three step method: (i) a synthetic solution without carbonate was prepared at room temperature under nitrogen atmosphere by dissolving chloride and sulfate salts in outgassed and boiled Milli-Q water; (ii) the Callovian-Oxfordian clay-rock sample was added to the solution, and (iii) the pH (initially at a value of ~8.1) was adjusted to a value of 7.2 by adding a hydrochloric acid solution (3.7 wt.%). The reactor was hermetically closed between each pH adjustment period. The third step was repeated until stabilization of the pH value to 7.2 (±0.15). A sample of the solution was filtered at 0.1 μm for initial composition analysis. The reactor was then hermetically sealed, and was heated at 80 °C ± 2 °C for the duration of the experiments. The advantage of this method was its simplicity, but the concentrations of ions such as calcium and chloride may be higher than expected initially due to HCl addition and calcite dissolution during the pH adjustment step.

In experiments 3 and 4, an alternative one-step method (Method 2) was applied with the use of a glove box filled with a N_2–CO_2 gas mixture (99–1 mol%; [O_2] < 1 ppm). The CO_2 partial pressure was close to equilibrium with the partial pressure at equilibrium of the clay-rock pore water at 25 °C (~10^{-2} bar) (Vinsot et al., 2008; Tournassat et al., 2015). The synthetic solution was prepared using chlorides, sulfates and bicarbonates salts. The pH of the solution stabilized rapidly in a few days to 7.3 (±0.1) at room temperature. The Callovian-Oxfordian clay-rock sample was added to the solution according to the experimental conditions described in Table 1. The pH measured after six days of equilibration in the N_2–CO_2 atmosphere was 7.3 ± 0.1 at room temperature. The reactors were then hermetically closed, and heated at 80 °C ± 2 °C.

During the experiments in Berghof reactors (not in the Parr pressure vessel), the partial pressure of CO_2, O_2, CH_4 and H_2S were monitored. At the end of the experiments in reactors, an-house designed device was used to extract the slurry from the reactor, under anoxic atmosphere, to measure the pH on-line in a flow cell at 80 °C immediately after extraction (to limit outgassing of the slurry), and to filter the slurry at 0.1 μm in an on-line filtration cell in an oven at 80 °C. For the experiment carried out in the Parr pressure vessel, the reactor was opened in a glove box under nitrogen atmosphere, then 3 mL of slurry was immediately sampled in a syringe, filtered at 0.1 μm, and injected in a hermetic vessel maintained at 80 °C for the pH measurement. The remaining slurry was filtered at 0.1 μm in a filtration cell at room temperature. After filtration, the solids were dried at 60 °C under nitrogen atmosphere for experiments 1 and 2, and were freeze-dried after freezing at −80 °C for the other two experiments. Solutions were analyzed for major cations (Ca^{2+}, Mg^{2+}, K^+, Na^+, Sr^{2+}) and anions (notably Cl^-, SO_4^{2-}), alkalinity, total carbon and dissolved inorganic carbon, minor and trace elements (notably Si, Al, Fe, Zn, Pb).

Table 1
Experimental conditions for the hydrothermal experiments.

Batch experiments	Synthetic solution preparation	Clay-rock sample mass (g)	Solution mass (g)	T (°C)	log $p_{CO2,init}$ (bar)	Duration (months)
Exp. 1	Method 1	21.0	227.7	79	−1.40	6
Exp. 2	Method 1	23.1	230.8	81	−1.46	20
Exp. 3	Method 2	23.0	227.4	81	−0.59	20
Exp. 4	Method 2	3.0	30.8	80	−1.46	21

Notes: see text for the description of methods 1 and 2 for preparing synthetic solutions at 25 °C under anoxic atmosphere. log $p_{CO2,init}$ values were measured the day after heating the reactors at 80 °C, except for reactor 3, for which it was measured after CO_2 was injected into the reactor at 80 °C. Experiments 1, 2 and 3 were carried out with the Berghof reactor, while experiment 4 was carried out with the Parr pressure vessel.

2.2.6. Solid characterization

2.2.6.1. Cation exchange. The cation exchange capacities and the cation populations on the exchanger were determined by using the chloride cobaltihexammine method as described in Gaucher et al. (2009). The duration for exchange with cobaltihexammine chloride solution was 1 h for all CEC and exchanged cations population measurements.

2.2.6.2. X-ray diffraction (XRD). Powder XRD patterns were recorded on a Bruker D8 Advance diffractometer, equipped with a Cu anode. Samples were preserved from the atmosphere during measurement by using a dome filled with N_2. Patterns were acquired in the 4–84°2θ CuKα range in continuous scan mode.

For clay mineral identification, the sample was first treated with acetic acid buffered by sodium acetate at pH 5 to remove carbonates and was Ca-saturated with 0.01 M $CaCl_2$, for 4–12 h at room temperature. This procedure was repeated four times to ensure saturation of the clay mineral interlayer by Ca^{2+}. The resulting suspension was then deposited on a glass side so as to obtain oriented Ca-saturated <2 μm fractions that were dried at room temperature for a few hours to obtain an air-dried (AD) preparation. Ethylene glycol (EG) solvation of these oriented slides was achieved by exposing them to ethylene glycol vapor for 12 h. XRD patterns of these oriented preparations were acquired in the 2–36°2θ CoKα angular range, in continuous scan mode, using a Siemens D5000 diffractometer equipped with variable slits, a Co anode and a diffracted beam monochromator.

2.2.6.3. Transmission electron microscopy (TEM). To prevent the alteration of phases that are prone to oxidation by atmospheric O_2 (i.e. pyrite) during sample preparation, the dispersion of the solid in ethanol and the drop deposit of the slurry on a carbon coated copper grid were carried out in a glove box under anoxic atmosphere ($O_2 < 1$ ppm per volume). Some preparations were also done under air condition for the observation of phases that are not sensitive to oxidation. Samples were observed with TEM before and after the hydrothermal experiments to detect chemical and/or morphological changes in primary minerals due to dissolution/precipitation processes, and also to identify potential neo-formed phases. The Philips CM20 apparatus, with 200 kV acceleration voltage and equipped with an LaB_6 filament, was coupled with an EDAX energy dispersive X-ray spectrometry using a Si(Li) detector.

2.2.6.4. ^{57}Fe Mössbauer spectrometry. The initial and final solids were analyzed with ^{57}Fe Mössbauer spectroscopy to detect possible changes in the distribution of Fe^{2+} and Fe^{3+} in pyrite, clay minerals and carbonates and to detect possible neo-formed iron oxides or (oxy)hydroxides. The apparatus was a constant acceleration Mössbauer spectrometer, in transmission geometry, using a ^{57}Co(Rh) source. The isomer shift values were corrected according to the calibration of the velocity scale made from α-Fe at 300 K. For each spectrum, the amount of Fe in the sample was about 5 mg·cm^{-2}. The obtained spectra were fitted using a discrete number of independent quadrupolar doublets composed of Lorentzian lines where the line width at half-height Γ (mm·s^{-1}), the isomer shift δ (mm·s^{-1}) and the quadrupole splitting ΔE_Q (mm·s^{-1}) were refined using a least-square fitting procedure.

2.2.6.5. Low-temperature magnetic measurements. These measurements were carried out on the final solids using a SQUID cryogenic magnetometer (Magnetic Properties Measurement System – MPMS) at the University of Kochi (Japan). This identifies magnetic minerals that show characteristic low temperature magnetic transitions, even if they are present at trace concentration (down to a few parts per billion per volume – ppbv). The measurement sequence used in this study was similar to those previously used on the initial solid (EST26479) and described in Kars et al. (2015). It consisted in a first cooling/warming 300–10–300 K cycle of a Saturation Isothermal Remanent Magnetization (SIRM), for which the value at 300 K is named M1. At 300 K, the sample was warmed to 400 K, above the Néel temperature of goethite (~393 K; Özdemir and Dunlop, 1996) and cooled down to room temperature in a 2.5 T magnetic field. At 300 K, the magnetic field was switched off. The remanence at this temperature step is called M2. Next the sample underwent a second 300–10–400 K cooling/warming cycle. At 400 K, all the remanence carried by goethite was removed. Finally, a 400–10–300 K cycle ended the sequence. The two last cycles were performed in a zero magnetic field. At the end of sequence, the obtained remanent magnetization is referred as M3. The difference between M2 and M3 is a proxy of the goethite concentration in the sample, as M2 is believed to concentrate all goethite and M3 is free of goethite (Guyodo et al., 2006). The maximum goethite concentration c_{goethite} (wt.%) was calculated according to the formula:

$$c_{\text{goethite}} = 100 \cdot \frac{M_2 - M_3}{M_{rs}} \quad (2)$$

where M_{rs} is the remanent magnetization at saturation for goethite, i.e. 0.05 A·m^2·kg^{-1}.

2.3. Cation exchange experiments

Cation exchange experiments were carried out at room temperature and 80 °C to determine the temperature dependence of cation exchange selectivity coefficients for the clay fraction of Callovian-Oxfordian samples. Na/K, Na/Ca, Na/Mg, Na/Sr exchange experiments and a five-element exchange experiment (Na–K–Ca–Mg–Sr) were performed with a total normality of ~0.005 mol·L^{-1} in chloride anionic background (Tournassat et al., 2007). The exchange selectivity coefficients were determined for an exchanger composition close to the one at equilibrium with the pore water composition at 25 °C and representative of the exchanger composition of Callovian-Oxfordian samples from the clay-rich C2b1 unit (Gaucher et al., 2004). The clay fraction sample was equilibrated with the synthetic solutions in polycarbonate bottles closed tightly with silicone seals, at 25 °C and 80 °C, and with solid to liquid ratios of 2.5 and 6.25 g·L^{-1}. Sealing tightness was checked

by weighing the reactors at the beginning and at the end of the experiments. After few days of equilibration, about 4 mL of solution were sampled and immediately filtered at 0.1 µm for solution composition analyses. The slurries in the reactors were then filtered at 0.1 µm at room temperature. In the case of experiments at 80 °C, the filtration duration was minimized by filtering small volumes of slurry and by renewing the filters regularly to prevent filter clogging. The filters with wet samples were precisely weighed on a 0.1 mg precision balance immediately after the filtration stages. They were weighed again after drying at 110 °C to determine the masses of residual solution in the samples after filtration. The quantity of exchanged cations Me with charges z per mass of dry clay ($q_{Me^{z+}}$, in mole of charge – mol_c – per kg^{-1}) were corrected by subtracting the contribution of cations in the remaining salts present in the solution soaking the clay to the measured cation concentrations, according to the following formula:

$$q_{\mathrm{Me}^{z+}} = z \times \frac{C_{extr}^{\mathrm{Me}^{z+}} \cdot V_{extr} - C_{sol}^{\mathrm{Me}^{z+}} \cdot V_{res}}{m_{clay}} \quad (3)$$

where $C_{extr}^{\mathrm{Me}^{z+}}$ is the concentration of Me measured in the cobalt hexamine extracting solution (in mol·L^{-1}), $C_{sol}^{\mathrm{Me}^{z+}}$ is the concentration of Me at equilibrium with the clay before extraction (in mol·L^{-1}), V_{extr} is the volume of extracting solution added to the solid after drying (in L), V_{res} is the volume of residual water in the solid after filtration and before drying (in L).

The cation exchange reactions occurring on the Na-saturated exchanger (clay fraction) were described with the following formalism:

$$z\mathrm{Na} - X + \mathrm{Me}_{(s)}^{z+} \rightleftharpoons \mathrm{Me} - \mathrm{X}_z + z\mathrm{Na}_{(s)}^{+} \quad (4)$$

where z is the charge of cation Me (Me = K^+, Ca^{2+}, Mg^{2+} or Sr^{2+}), X^- is the solid exchanger and (s) denotes ions in the solution phase. Considering this reaction, the exchange selectivity coefficient $K_{ex}^{Na/Me}$ in the Gaines and Thomas convention (Gaines and Thomas, 1953) is expressed by:

$$K_{ex}^{\mathrm{Na/Me}} = \frac{E_{\mathrm{Me}}[\mathrm{Na}^+]^z}{(E_{\mathrm{Na}})^z[\mathrm{Me}^{z+}]} \quad (5)$$

where E_{Me} and E_{Na} are the equivalent fractions of Me^{z+} and Na^+ on the exchanger, $[Na^+]$ and $[Me^{z+}]$ are the activities of the cations Na^+ and Me^{z+} in solution.

Uncertainties (u) on the exchanged cation contents and on the Gaines and Thomas selectivity coefficients were estimated from Eqs. (3) and (4) with the following uncertainties applied to the main parameters: $u(C_{extr}^{Me^{z+}}) = 2\% \times C_{extr}^{Me^{z+}}$, $u(C_{sol}^{Me^{z+}}) = 2\% \times C_{sol}^{Me^{z+}}$, $u(V_{res}) = 10\% \times V_{res}$ and $u([\mathrm{Me}]) = 2\% \times [\mathrm{Me}]$. The uncertainties on the mass of clay sample and the volume of the extracting solution were neglected. By also neglecting the covariance between parameters, we obtain (Danzer, 2007):

$$u(q_{\mathrm{Me}^{z+}}) = \frac{z}{m_{clay}} \sqrt{\begin{array}{l}(V_{extr}+V_{res})^2 u(C_{extr}^{\mathrm{Me}^{z+}})^2 + (C_{extr}^{\mathrm{Me}^{z+}})^2 u(V_{res})^2 \\ +V_{res}^2[u(C_{sol}^{\mathrm{Me}^{z+}})]^2 + (C_{sol}^{\mathrm{Me}^{z+}})^2 u(V_{res})^2\end{array}} \quad (6)$$

$$u(K_{ex}^{NaMe_{div}})^2 = \left[\frac{[Na^+]^2}{[Me_{div}^{2+}]}\frac{(q_{Na}+2q_{Me_{div}})}{q_{Na}^2}\right]^2 u(q_{Me_{div}})^2 + \left[\frac{[Na^+]^2}{[Me_{div}^{2+}]}\frac{q_{Me_{div}}\left(1+\frac{2q_{Me_{div}}}{q_{Na}}\right)}{q_{Na}^2}\right]^2 u(q_{Na})^2 + \left[\frac{[Na^+]}{[Me_{div}^{2+}]}\frac{2q_{Me_{div}}(q_{Na}+q_{Ca})}{q_{Na}^2}\right]^2 u([Na^+])^2 + \left[\frac{[Na^+]^2}{[Me_{div}^{2+}]^2}\frac{q_{Me_{div}}(q_{Na}+q_{Ca})}{q_{Na}^2}\right]^2 u([Me_{div}^{2+}])^2 \quad (7)$$

$$u(K_{ex}^{NaK})^2 = \left(\frac{1}{q_{Na}}\frac{[Na^+]}{[K^+]}\right)^2 u(q_K)^2 + \left(\frac{q_K}{q_{Na}^2}\frac{[Na^+]}{[K^+]}\right)^2 u(q_{Na})^2 + \left(\frac{q_K}{q_{Na}}\frac{1}{[K^+]}\right)^2 u([Na^+])^2 + \left(\frac{q_K}{q_{Na}}\frac{[Na^+]}{[K^+]^2}\right)^2 u([K^+])^2 \quad (8)$$

where Me_{div} = Ca, Mg or Sr.

2.4. Thermodynamic modeling

Experimental results were modeled using a thermodynamic and kinetic approach. Geochemical calculations were performed with PHREEQC version 3 (Parkhurst and Appelo, 1999, 2013) using the Thermochimie (Giffaut et al., 2014) or the Thermoddem (Blanc et al., 2012) databases for thermodynamic data.

3. RESULTS

3.1. Predicted pore water compositions

The pore water compositions predicted with the two different databases and the two scenarios described in the previous section are given in Table 2, together with the considered mineral assemblages. In both scenarios, an increase in temperature leads to a decrease in pH and an increase in p_{CO2}. The amplitude of pH and p_{CO2} changes was greater for the scenario where clay minerals were taken into account in the calculation highlighting the potential contribution of clay minerals in regulating the pH value (Gaucher et al., 2006, 2009). The concentration changes were otherwise limited with the exception of Al and Si concentrations, for which a significant increase was predicted by the model with the full mineralogical assemblage. Otherwise, the use of the Thermochimie or of the Thermoddem database had little influence on the predicted composition with the notable exception of sulfate concentration for which a decrease due to a precipitation of celestite ($SrSO_4$) was predicted by the calculation with the Thermoddem database.

3.2. Hydrothermal experiments results – gas phase composition

The measured p_{O2} values were lower than the detection limit (<0.001 vol.%) for experiments 1 and 2, showing good sample preservation from the contact with atmospheric O_2. For experiment 3, p_{O2} values ranged from 0.01 vol.% to 0.1 vol.%. O_2 probably entered the system during the injection of CO_2 at the beginning of this experiment. The p_{CH4} and p_{H2S} values were always lower than the detection limits

Table 2
Compositions of the synthetic solutions calculated at 25 °C and 80 °C and prepared for hydrothermal experiments, and comparison with compositions measured at the end of the hydrothermal experiments (n.d. = not determined). For major elements the uncertainty on the measured concentrations was estimated to be ±5 %.

Reference	T	pH	p_{CO2}	Concentrations (mmol/L)											
	(°C)		(bar, $\log_{10}$)	Ca	Mg	Na	K	Cl	SO_4	Sr	DIC	Alk.	Fe	Al	Si
Modeled pore water composition at 25 °C, full mineralogy[*]															
Gaucher et al., 2009	25	7.2	−2.2	8.5	5.4	43	1.0	41	15	0.21	2.4		0.047	$3.0 \cdot 10^{-5}$	0.18
This study, Thermochimie	25	7.1	−2.0	8.6	5.8	43	1.0	41	15	0.20	3.2	2.9	0.048	$7.2 \cdot 10^{-5}$	0.18
This study, Thermoddem	25	7.1	−1.9	8.6	5.7	43	1.0	41	15	0.21	3.4	3.1	0.077	$6.3 \cdot 10^{-5}$	0.18
Modeled pore water composition at 80 °C, mineralogy restricted to fast reacting mineral phases[**]															
This study, Thermochimie	80	6.5	−1.2	12	3.2	42	1.0	41	15.0	0.23	2.9	2.2	0.061	–	–
This study, Thermoddem	80	6.5	−1.1	9.8	2.8	39	0.96	41	11	0.17	2.9	1.9	0.081	–	–
Modeled pore water composition at 80 °C, full mineralogy[*]															
This study, Thermochimie	80	6.0	−0.29	12	3.4	43	1.0	41	15	0.26	11	5.7	0.068	$5.8 \cdot 10^{-4}$	0.69
This study, Thermoddem	80	6.0	−0.24	10	2.8	40	0.99	41	11	0.19	12	5.0	0.086	$5.1 \cdot 10^{-4}$	0.70
Initial and final compositions of solution in hydrothermal experiments															
Exp. 1, initial	21	7.1	−2.2	20	4.8	44	2.5	68	11	0.32	2.5	n.d.	0.021	$5.7 \cdot 10^{-4}$	0.28
Exp. 1, 6 months[***]	79	6.6	−1.3	23	5.3	50	2.8	84	13	0.27	1.0	2.1	$2.0\ 10^{-3}$	$6.2 \cdot 10^{-4}$	0.62
			−1.3	*18*	*4.3*	*41*	*2.3*	*68*	*11*	*0.22*	*0.8*	*1.7*	*1.6 10⁻³*	*5.0 · 10⁻⁴*	*0.50*
Exp. 2, initial	21	7.3	−2.5	12	4.3	46	1.7	44	11	n.d.	2.0	n.d.	$4.0\ 10^{-3}$	$2.9 \cdot 10^{-4}$	0.13
Exp. 2, 20 months[***]	81	6.7	−1.1	10	3.6	47	1.8	50	12	0.14	1.2	1.5	$6.5\ 10^{-3}$	$3.6 \cdot 10^{-4}$	0.67
			−1.1	*8.8*	*3.2*	*41*	*1.6*	*44*	*10*	*0.12*	*1.1*	*1.3*	*5.7 10⁻³*	*3.2 · 10⁻⁴*	*0.59*
Exp. 3, initial	21	7.3	−2.1	7.8	6.6	47	1.4	44	17	0.21	n.d.	5.3	$1.1\ 10^{-4}$	$5.1\ 10^{-4}$	0.21
Exp. 3, 20 months	81	6.7	−0.9	8.4	6.2	53	1.8	49	18	0.17	1.1	3.2	$5.3\ 10^{-4}$	$2.8 \cdot 10^{-4}$	0.52
Exp. 4, initial	21	7.3	n.d.	7.5	6.5	47	1.4	46	18	0.23	n.d.	3.3	$1.6\ 10^{-4}$	$6.8 \cdot 10^{-4}$	0.14
Exp. 4, 21 months	80	6.9	−1	8.1	6.9	52	1.7	48	19	0.21	2.8	2.5	$2.1\ 10^{-4}$	$3.4 \cdot 10^{-4}$	0.64

[*] Mineralogical assemblage: celestite, calcite, dolomite, siderite, quartz, pyrite, chlorite-Cca2 (Ripidolite-CCa2 in Thermochimie), illite-IMt2 + cation exchange.
[**] Mineralogical assemblage: celestite, calcite, dolomite, siderite + cation exchange.
[***] The second line corresponds to value corrected from water evaporation during the sampling and measurement procedure.

for all experiments. The evolution of p_{CO2} as a function of time for experiments 1, 2 and 3 is given in Fig. 2. In experiments 1 and 2, the p_{CO2} reached rapidly values at about $10^{-1.4}$ and $10^{-1.2}$ after initial heating at 80 °C. The p_{CO2} increased slightly afterwards, up to $10^{-1.3}$ and $10^{-1.1}$ bar after 20 months of interaction for experiments1 and 2 respectively. In experiment 3, the p_{CO2} followed the same trend as in experiment 2 before the CO_2 injection. After the injection of CO_2 into the reactor and a rapid increase up to $10^{-0.6}$ bar, the p_{CO2} first decreased rapidly from $10^{-0.55}$ to $10^{-0.7}$ bar. This decrease was mainly due to the dissolution of CO_2 from the gas phase into the solution. Afterwards, the p_{CO2} tended to remain stationary with eventually a small decrease, down to $10^{-0.9}$ bar at 20 months.

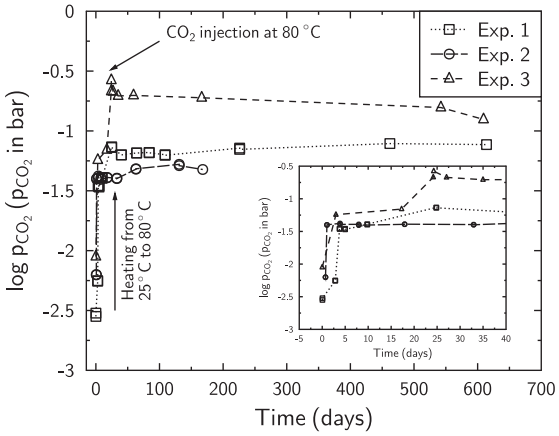

Fig. 2. Evolution of the partial pressure of CO_2 (in bar) as a function of time for the experiments at 80 °C in reactors. The initial p_{CO2} correspond to the p_{CO2} at near-equilibrium with the water/-clay-rock system at 25 °C ($10^{-2.5}$–10^{-2} bar). The CO_2 overpressure of $10^{-0.6}$ bar measured in experiment 3 corresponds to the CO_2 injection. The inset is a zoom on the evolution of the p_{CO2} during the first 40 days of the experiments, showing the short duration of the initial heating period. Error bands are smaller than the symbols.

3.3. Hydrothermal experiments results – solution composition

For experiments 1 and 2, significant discrepancies were noticed between the initial and final chloride concentrations (+19 % and +12 % respectively) although chloride ions were not expected to contribute to chemical processes in the investigated system. The assumption of a leakage during the experiment was discarded considering how stable the total pressure monitored was between each gas sampling event over the six month and twenty month periods.

For experiment 1, this discrepancy was due to an experiment issue that occurred during the final stage of extraction

and filtration of the suspension at 80 °C, and that generated a significant evaporation artifact. To circumvent this problem, the measured concentrations were corrected by using a factor corresponding to the normalization with respect to chloride concentration. For experiments 3 and 4, the measured concentrations were not corrected, since the differences between initial and final chloride concentrations were within the order of magnitude of the error on the analytical measurements.

The final compositions of the solutions after 20 months of interaction with the solid at 80 °C were similar for experiments 2, 3 and 4 (Table 2). More importantly, with the exception of pH, p_{CO2} and Si concentration, the changes in composition of the solution between the initial and final measurements were very limited for the four experiments.

3.4. Hydrothermal experiments results – solid characterization

Powder XRD patterns of all initial and reacted samples had a high degree of similarity (Fig. 3). The sole significant differences that could be observed are the presence of a broad maximum at ~6 °2θ CuKα in sample Exp3 – 20 m, which is typical for interstratified clay minerals and probably results from sample heterogeneity, and the presence of a weak diffraction maximum at ~13.7 2θ CuKα in sample Exp3 – 20 m and Exp4 – 21 m, whose origin remains unclear. XRD patterns acquired on oriented slides were also similar for all samples (Fig. 4), thus validating that the high abundance of interstratified clay minerals in the powder pattern of sample Exp3 – 20 m was due to a sampling artifact. The positions of the reflections in the air-dried state and their evolution upon saturation with ethylene–glycol were similar for all samples. This, associated with the fact that no systematic variation with time could be observed, pleads for the absence of change in the clay mineralogy during the course of the experiments. Following previous studies (Claret et al., 2004), the presence of illite, smectite and randomly interstratified illite–smectite could be identified.

Coherently with XRD, TEM-EDX analyses revealed only few changes in the mineralogy during the hydrothermal experiments. The first main observation was the detection of crystals of goethite, identified on selected-area electron diffraction (SAED) patterns, on the samples having undergone twenty months of equilibration at 80 °C. These crystals exhibited an acicular morphology with needles of 100–500 nm length (Fig. 5). The needles were mostly assembled in isolated clusters, but were also observed in association with pyrite grains, were they seemed to have undergone epitaxial growth (Fig. 5c). Traces of nanocrystalline goethite had been detected in the initial sample, preserved from air since its collection, (Kars et al., 2015). However, this nanocrystalline goethite could never be observed

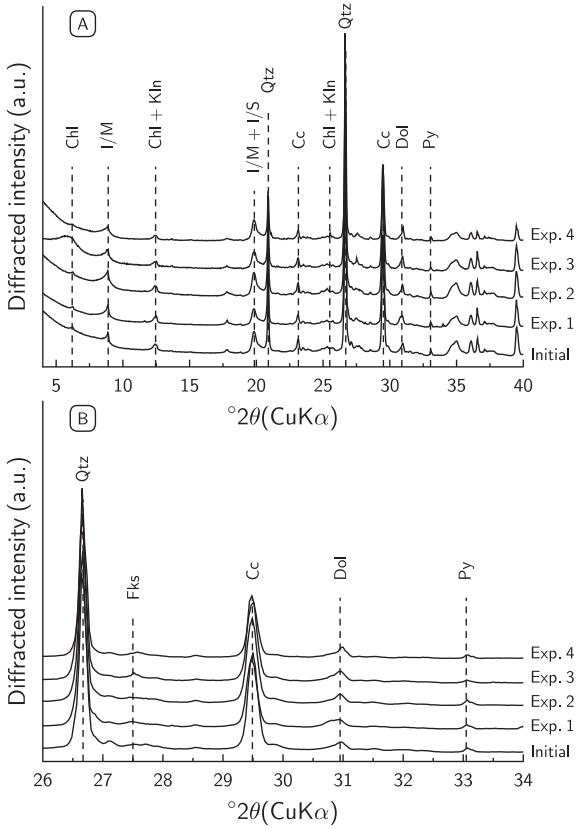

Fig. 3. Experimental XRD patterns on Callovian-Oxfordian powder samples acquired on the initial sample and on the samples reacted at 80 °C (a) between 4 and 40° 2θ and (b) zoom between 26 and 34° 2θ. Peak positions are outlined as dashed lines for illite/mica (I/M), chlorite (Chl), kaolinite (Kln), mixed-layer illite/smectite (I-S), quartz (Qtz), K-feldspar (Kfs), calcite (Cc), dolomite (Dol) and pyrite (Py).

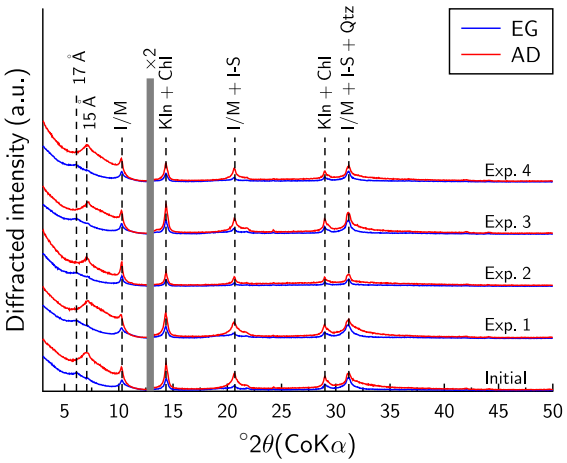

Fig. 4. Experimental XRD patterns (oriented slides, decarbonated and Ca-saturated <2 μm size fraction) of the initial sample and of the samples reacted at 80 °C. The red and blue solid lines represent patterns recorded in the air-dried (AD) state and after ethylene glycol (EG) solvation, respectively. Peak positions are outlined as dashed lines for illite/mica (I/M), chlorite (Chl), kaolinite (Kln), mixed-layer illite/smectite (I-S) and quartz (Qtz) contributions. The vertical gray bars indicate a modified scale factor for the high-angle regions compared to the 2–13° 2θ angular range. XRD intensities were normalized from I/M intensity at 10.2° 2θ. (For interpretation of the references to color in this figure legend, the reader is referred to the web version of this article.)

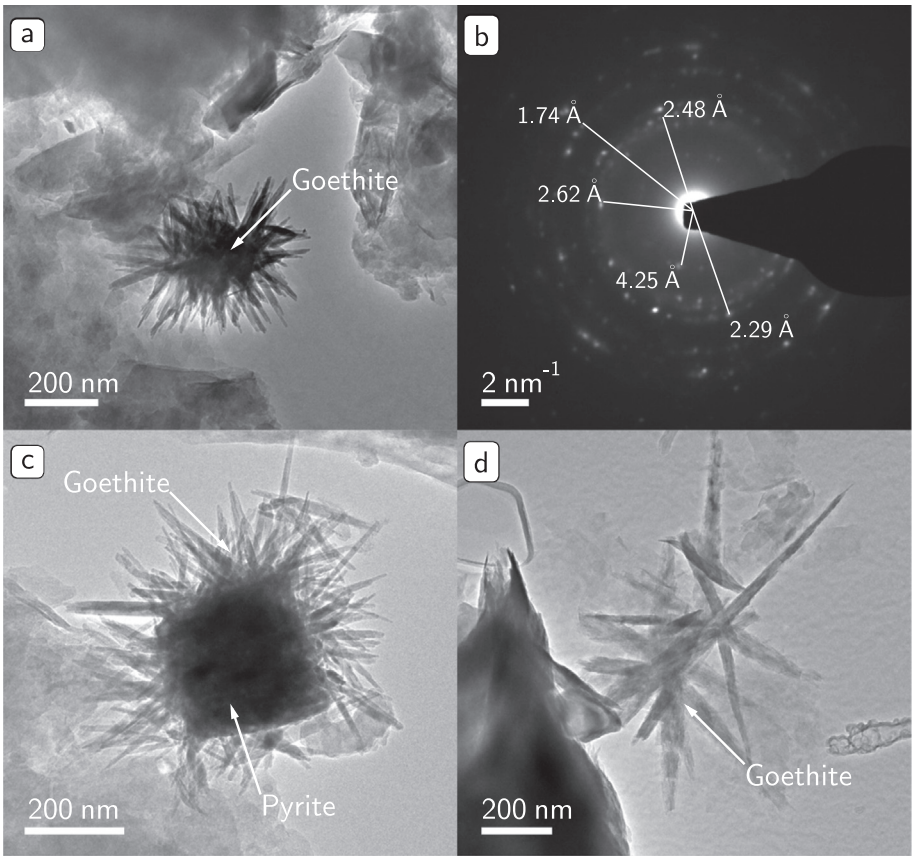

Fig. 5. TEM micrographs and identification of neo-formed goethite in samples reacted at 80 °C for 20 months in an anoxic atmosphere. (a) and (b) image of goethite and its associated SAED pattern (reflections corresponding to d_{101}, d_{111}, d_{301}, d_{212}, d_{211}) (Chichagov, 1994); (c) and (d) images of goethite crystals with acicular morphologies.

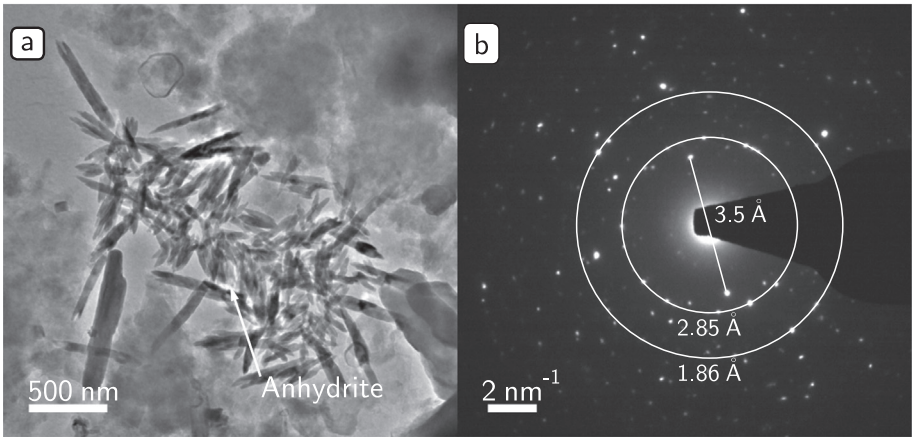

Fig. 6. Neo-formed anhydrite observed in samples reacted at 80 °C for 20 months in an anoxic atmosphere: (a) TEM image and (b) SAED pattern (reflections corresponding to d_{200}, d_{102} and d_{302} of anhydrite (Chichagov, 1994); other reflections result from all surrounding matrix minerals).

directly with TEM. In samples reacted at 80 °C, the goethite crystals could be easily imaged and were most probably neo-formed. The second main observation was the presence of anhydrite ($CaSO_4$) in the final solids after twenty months of equilibration at 80 °C (Fig. 6). The crystals, with stick morphology and sub-micrometric sizes, were mostly aggregated. Similarly to acicular goethite crystals, anhydrite crystals were probably neo-formed phase since

they could not be observed by TEM-EDX in the initial sample, and both were probably present at trace concentration in the solid, as they could not be detected by XRD. TEM-EDX analyses performed on the final samples did not evidence the presence of other neo-formed phase. The analyses of kaolinite, feldspar and dolomite particles were consistent with those of the mineral in the initial sample (Fig. 7).

The ^{57}Fe Mössbauer spectra for the initial and final samples from experiments 1 and 2 are shown in Fig. 8. The values of Mössbauer parameters extracted from spectral modeling are given in Table 3. The doublet structural attributions were made according to previous studies (Tournassat et al., 2008; Didier et al., 2014). Samples at 6 and 20 months showed enriched Fe^{2+} associated to clay minerals corresponding to depleted Fe^{2+} associated to pyrite and/or depleted Fe^{3+} in the structure of clay minerals. We could not detect any magnetic sextuplets corresponding to rather large grain (>20 nm) of goethite precipitation in Mössbauer spectra that were acquired in the −4 to +4 mm·s^{-1} window.

The low-temperature magnetic properties were measured on the final samples from experiments 3 and 4, and compared with those of the initial sample (Kars et al., 2015) (Fig. 9). For the final sample from experiment 3 (Fig. 9 a), the cooling of the room temperature SIRM (RT-SIRM) during cycle 1 showed increased magnetization by about a factor 1.8 between 300 K and 40 K, suggesting the occurrence of goethite (Dekkers, 1989). The cooling and warming curves were not reversible from ~110 K, suggesting the presence of coarse-grained (Ti)-magnetite with Verwey temperature at ~120 K (Muxworthy and McClelland, 2000; Özdemir et al., 2002). The measured M2 ($1.32 \cdot 10^{-4}$ A·m^2·kg^{-1}) was very close to M1 ($1.31 \cdot 10^{-4}$ A·m^2·kg^{-1}), suggesting that the heating/cooling step in a 2.5 T field in the 300–400 K temperature range did not mobilize more magnetic grains. The increased remanence during the cooling in cycle 2, between 300 and 40 K, was on the same order of magnitude as in cycle 1. Similarly to cycle 1, the cooling and warming curves in cycle 2 were not reversible, indicating coarse-grained (Ti-) magnetite. The remanence during cycle 3 was much lower than during the previous cycles, suggesting that most of the goethite signal had been removed. Nevertheless ~75 % of the remanence remained at the end of cycle 3, confirming the presence of other magnetic minerals with Néel/Curie temperature higher than 400 K (e.g. magnetite, hematite).

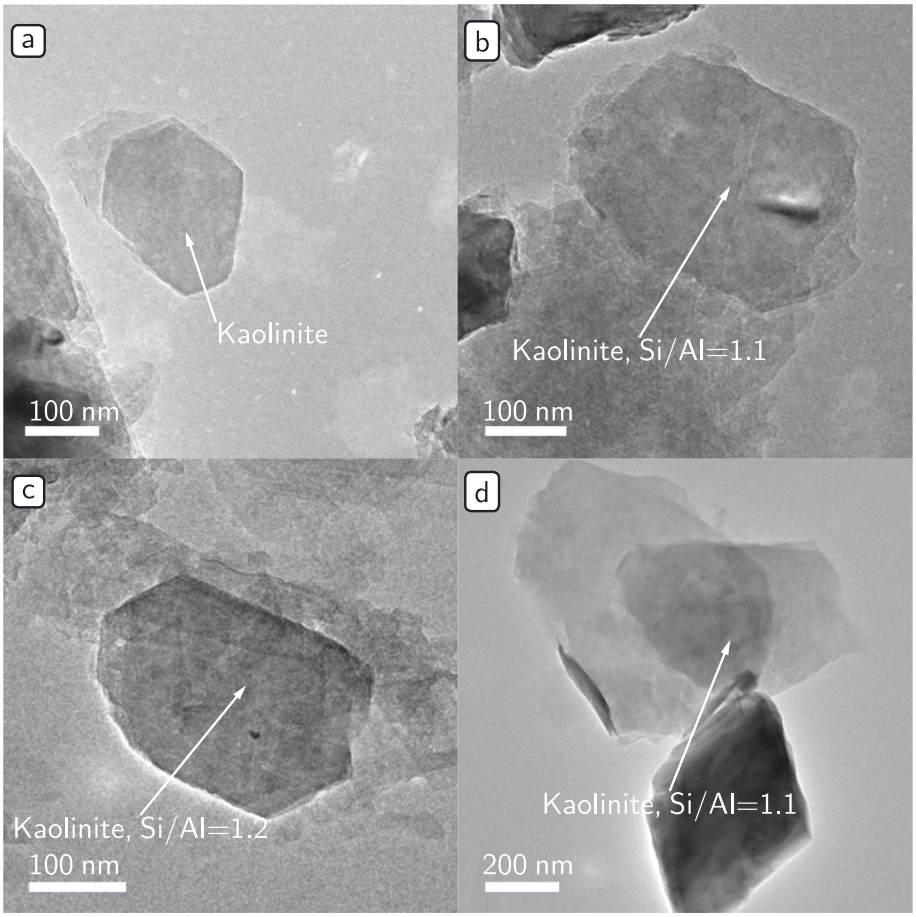

Fig. 7. TEM micrographs of kaolinite in the samples: (a) and (b) thin particles observed in the initial clay-rock sample; (c) and (d) particles in the samples reacted at 80 °C for 20 months in an anoxic atmosphere.

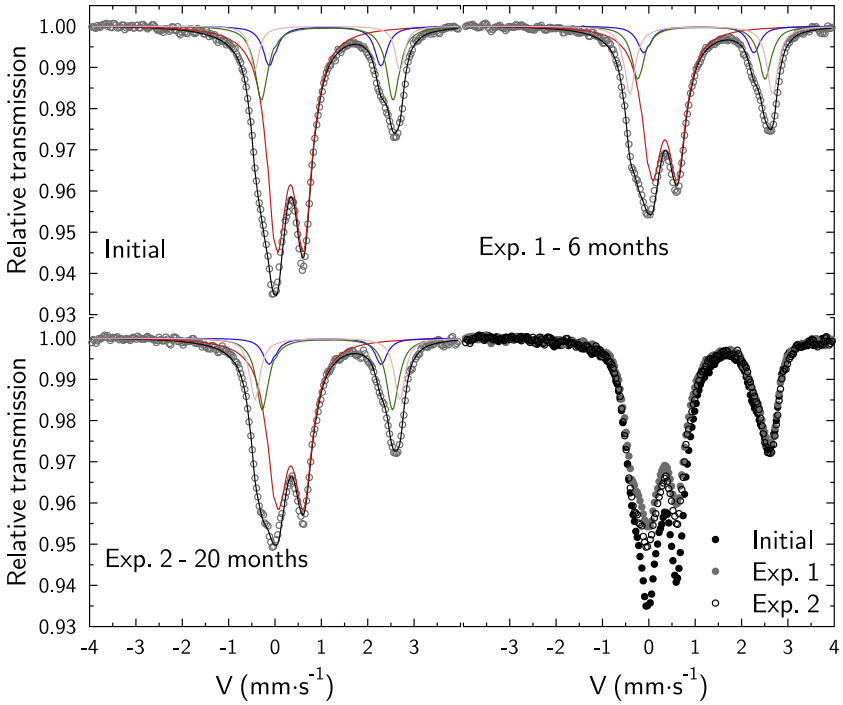

Fig. 8. 77 K Mössbauer spectra of initial sample EST 26479 and samples from experiments at 6 months (Exp. 1) and 20 months (Exp. 2) at 80 °C. Circles correspond to measurements. Red, pink, green and blue curves refer to Mössbauer fitting components given in Table 3. The black curve is the sum of all of these contributions. (For interpretation of the references to color in this figure legend, the reader is referred to the web version of this article.)

Table 3
Mössbauer parameters at 77 K for EST 26479 initial sample, 6-month sample (from Exp. 1) and 20-month sample (from Exp. 2).

Sample	Doublets	I.S. ($mm·s^{-1}$)	Γ ($mm·s^{-1}$)	ΔE_Q ($mm·s^{-1}$)	%	Doublet structural attributions
Initial sample	1 (red)	0.44	0.46	0.56	65	Fe^{2+} in pyrite and/or Fe^{3+} in clay minerals
	2 (blue)	1.20	0.32	2.38	9	Fe^{2+} in carbonate
	3 (green)	1.25	0.35	2.81	18	Fe^{2+} in octahedral sheets of clay minerals or adsorbed on clay
	4 (pink)	1.25	0.24	3.10	8	mineral surfaces
Exp. 1	1 (red)	0.45	0.46	0.54	58	Fe^{2+} in pyrite and/or Fe^{3+} in clay minerals
(6 months)	2 (blue)	1.20	0.32	2.35	8	Fe^{2+} in carbonate
	3 (green)	1.26	0.33	2.71	16	Fe^{2+} in octahedral sheets of clay minerals or adsorbed on clay
	4 (pink)	1.26	0.29	3.05	18	mineral surfaces
Exp. 2	1 (red)	0.44	0.48	0.55	59	Fe^{2+} in pyrite and/or Fe^{3+} in clay minerals
(20 months)	2 (blue)	1.20	0.32	2.39	7	Fe^{2+} in carbonate
	3 (green)	1.25	0.33	2.78	20	Fe^{2+} in octahedral sheets of clay minerals or adsorbed on clay
	4 (pink)	1.25	0.28	3.09	14	mineral surfaces

I.S. = Isomer shift value relative to that of the α-Fe at 300 K; Γ = line width; ΔE_Q = quadrupolar splitting value; % = ratio of each component.

In final sample from experiment 4 (Fig. 9b), M1 was $7.9 \cdot 10^{-5}$ $A·m^2·kg^{-1}$, which was lower than in experiment 3. Between 300 and 40 K, the remanence increased by a factor of ~2.2 compared to experiment 3. The remanence was not fully recovered during warming from ~120 K that corresponds to the Verwey transition of magnetite. M2 ($8.9 \cdot 10^{-5}$ $A·m^2·kg^{-1}$) was higher than M1, suggesting that more grains were mobilized. Cycle 2 showed the same characteristics as cycle 1 (signal increased by a factor 2.2, no curve reversibility). Eighty-four percent of the magnetization signal remained after cycle 3, suggesting the presence of other magnetic minerals.

Both samples from experiments 3 and 4 showed a large increase in magnetization below 40 K on the RT-SIRM curves (Fig. 9a and b), suggesting the presence of a strong paramagnetic component in the samples, which generates

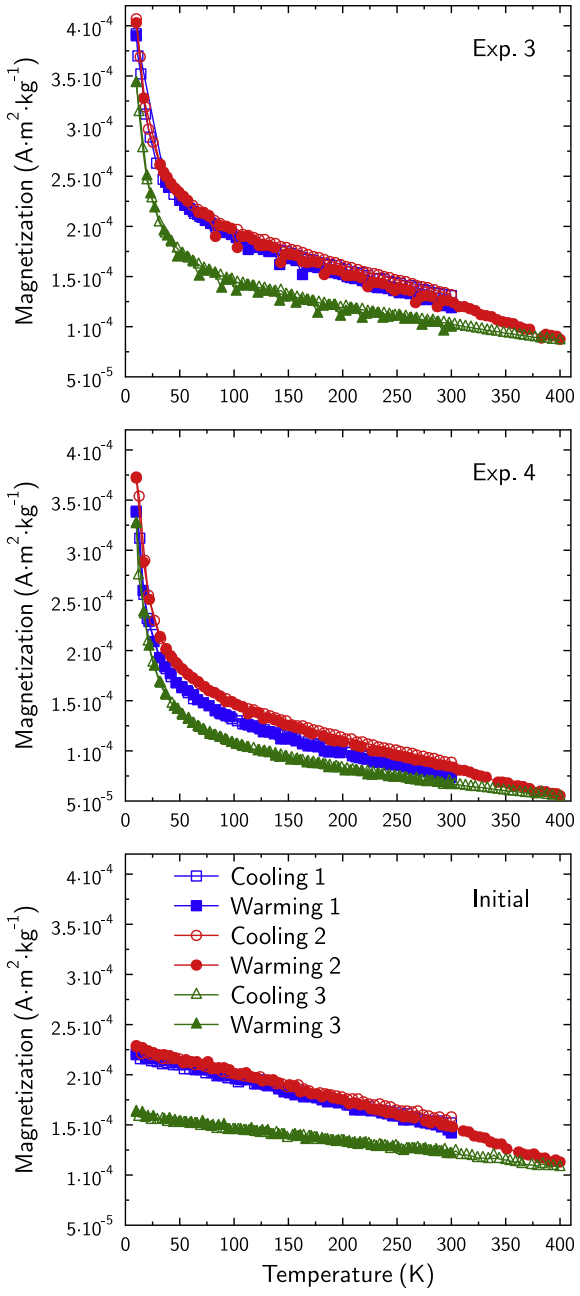

Fig. 9. Evolution of the room temperature saturation isothermal remanent magnetization for the two final samples from experiments 3 and 4, compared to initial sample (Kars et al., 2015) during three successive cooling-warming cycles. The increase in remanence from 300 to 10 K is 75 % and 73 % for cycles 1 and 2. Note that for all the samples (initial and final) the remanence is not entirely removed after the last heating step at 395 K (cycle 3).

an induced magnetization as a result of a residual magnetic field trapped inside the magnetic properties measurement system (~2 Oersted). The paramagnetic component could be clay minerals, but also other minerals such as siderite which is paramagnetic at room temperature but becomes antiferromagnetic below its Néel temperature at ~38 K (Housen et al., 1996; Frederichs et al., 2003; Kars et al., 2015). To test the presence of siderite, complementary low temperature measurements were carried out. A SIRM was imparted at 5 K and the evolution of the remanence was monitored during warming to 300 K. Both samples from experiments 3 and 4 showed a well-marked break-in-slope at ~37–39 K (data not shown). This finding suggests the presence of siderite in the samples.

By comparison with the initial sample (Fig. 9c), most of the magnetic properties of the final samples from experiments 3 and 4 were preserved. Final and initial samples did not show significant shifts between cycles 1 and 2, suggesting that the heating/cooling step in a 2.5 T field in the 300–400 K temperature range mobilized the same amount of magnetic grains. Goethite and minor magnetite remained the major magnetic phases in final samples, but the presence of siderite in final samples was highly probable. The maximum goethite concentrations in Experiments 3 and 4 were about 0.07 wt.% and 0.05 wt.% respectively, which are values very similar to the pristine sample.

3.5. Cation exchange results

Results for exchanged cations population measurements corrected from the contribution of residual salts are given in Table 4. The compositions of the exchanger were quite similar for solids collected from experiments 3 and 4. The exchanger composition from experiment 2 was enriched in Ca^{2+} and depleted in Mg^{2+} compared to the exchanger composition from experiments 3 and 4. The presence of very significant NH_4^+ can be attributed to the reductive degradation of part of the cobaltihexammine molecules during the exchange experiment, and is indicative of good preservation of the redox properties of the clay-rock samples (Hadi et al., 2016).

Results for exchange selectivity coefficients at 25 °C and 80 °C are shown in Fig. 10. Error bands are representative of a coverage factor of $k = 2$ (corresponding approximately to an *a priori* confidence level of ~95 %). The results were similar for both solid to liquid ratios (S/L). The values of exchange selectivity coefficients are summarized in Table 5 for Na/K, Na/Ca, Na/Mg, Na/Sr and Na-K-Ca-Mg-Sr exchange experiments. The Na/Ca, Na/Mg and Na/Sr exchange coefficients remained essentially constant as a function of temperature in the limit of the error bands. The Na/K selectivity coefficient slightly decreased from $10^{1.1}$ at 25 °C to 10^{1} at 80 °C. It was changed accordingly in the cation exchange database for calculations related to 80 °C.

4. MODELING AND DISCUSSION

4.1. Mineralogical changes in presence of a 80 °C thermal perturbation

The thermal perturbation of the clay-rock samples led to very limited mineralogical changes. This result is in agreement with previously reported results obtained in similar experimental conditions from Beaucaire et al. (2012). From the modeling of XRD patterns on the <0.1 μm size fraction after 15 months, those authors detected only subtle changes

Table 4
Exchanged cations populations measured on final solids and corrected for the contribution of residuals salts. Uncertainties on the quantity of exchanged cations per mass of dry clay were calculated with a coverage factor of $k = 2$ (see Eq. (6)).

Experiment	Exchanged cations population ($mmol_c \cdot kg^{-1}$)						Sum of exchanged cations (excluding NH_4^+) ($mmol_c \cdot kg^{-1}$)
	Na^+	K^+	Ca^{2+}	Mg^{2+}	Sr^{2+}	NH_4^+	
Exp. 1	n.d.	n.d.	n.d.	n.d.	n.d.	n.d.	n.d.
Exp. 2	19 (±8)	16 (±1)	130 (±7)	24 (±2)	6 (±0.3)	67 (±3)	195 (±18)
Exp. 3	32 (±7)	15 (±1)	99 (±6)	52 (±3)	4 (±0.2)	25 (±1)	202 (±17)
Exp. 4	14 (±9)	14 (±1)	94 (±6)	53 (±4)	4 (±0.2)	20 (±1)	179 (±21)

n.d. : not determined.

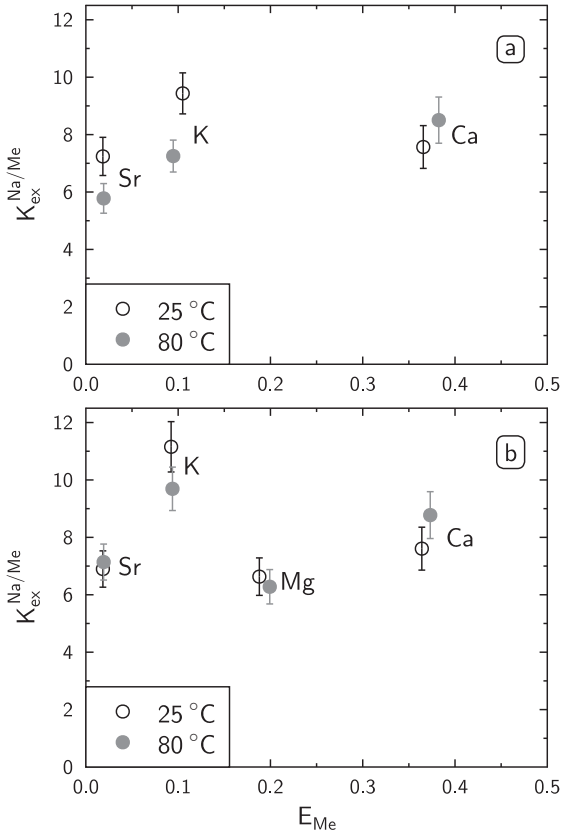

Fig. 10. Gaines and Thomas selectivity coefficients for Na–Me (Me = K, Ca, Mg, Sr) exchange on the clay fraction (<2 μm) of K119 sample determined from Na-Me exchange experiments at 25 and 80 °C. The equivalent fractions of Me cations on the exchanger, E_{Me}, are representative of the cation exchanger composition of a Callovian-Oxfordian sample in the clay-rich zone C2b1. Experiments with (a) S/L = 6.25 g/L; (b) S/L = 2.5 g/L.

in the clay mineral proportions and structures, with an increase of less than 5 % in illite layers. They attributed these changes to the collapse of the expandable layers in mixed-layer minerals rather than by the increase in the illite phase content. From TEM-EDX analysis results, Beaucaire et al. (2012) also suspected the presence of neo-formed Si enriched kaolinite particles. However, very thin particles of kaolinite with a typical hexagonal morphology could also be observed in our non-reacted samples (compare our Fig. 7 and Fig. 5-B3 in Beaucaire et al., 2012). Although the formation of kaolinite during a thermal perturbation cannot be discarded, there is no clear evidence that it indeed occurred. Beaucaire et al. (2012) reported the presence of neo-formed Ca/Mg carbonate with round edges in their final solids. The Ca/Mg carbonate shown by the authors did not exhibit the expected rhombohedral morphology that is typical of a euhedral crystal of calcite or dolomite (Fig. 11). Among the few Ca/Mg carbonates that could be detected in our samples, only dolomite particles with Ca/Mg ratio that were consistent with those measured in the initial sample (Ca/Mg ~ 0.8–1) were observed. These ratios were also consistent with those previously measured in Lerouge et al. (2011) on unreacted samples from other cores from the Callovian-Oxfordian Formation (see Fig. 11). Again, although the neo-formation of dolomite (or Ca/Mg carbonates) in the presence of a thermal perturbation cannot be discarded, solid analysis did not provide clear evidence of it. Also, we observed no significant change in K-feldspars chemical compositions and morphologies between initial and reacted samples, in agreement with the observations of Beaucaire et al. (2012).

From the above analysis, it is clear that the reactivity of the carbonate and alumino-silicate systems cannot be easily constrained on the basis of the post-mortem solid analysis. This difficulty can be appreciated by taking a closer look at predictive modeling calculations. For modeling purposes, the mineralogical assemblage given in Table 6 was considered to be representative of the mineralogical assemblage of the initial clay-rock sample. We took the initial composition of the solution, the solid to liquid ratio and the presence of a gas phase as input parameters, and we carried out calculations at thermodynamic equilibrium with the Thermochimie database (Giffaut et al., 2014) for the two scenarios presented in the materials and methods section (fast reacting system and whole system, see Table 2). The calculation results for the experiment 2 are listed in Table 6 (The results and interpretations for experiments 1, 3 and 4 were essentially the same as for experiment 2). In the fast-reacting system scenario (with carbonates, sulfates and cation exchanger only), the modeled variations of mineral amounts were too low to be quantified unambiguously if one considers the error bands associated with mineralogical analysis and with the variability induced by the sampling procedures. In the "whole system" scenario, only dolomite, siderite and chlorite could undergo large variations relative to their initial amount (−36 %, −50 %, and +100 % respectively). We must stress that in the model, siderite represents the presence of Fe-rich carbonates with very variable com-

Table 5
Exchange selectivity coefficients (Gaines and Thomas convention) obtained on the <2 μm clay fraction at room temperature and 80 °C and comparison with literature data.

Exchange exp.	T	Equivalent fraction of cation on the exchanger					Gaines and Thomas exchange selectivity coefficients (log_{10} scale)			
	(°C)	E_{Na}	E_K	E_{Ca}	E_{Mg}	E_{Sr}	Na/K	Na/Ca	Na/Mg	Na/Sr
Na/K	Room	0.85	0.09	0.01	0.05	0.00	1.05 (±0.03)			
	80	0.83	0.09	0.01	0.07	0.00	0.99 (±0.03)			
Na/Ca	Room	0.52	0.07	0.36	0.05	0.00		0.88 (±0.04)		
	80	0.49	0.07	0.37	0.06	0.00		0.94 (±0.04)		
Na/Mg	Room	0.73	0.07	0.01	0.19	0.00			0.82 (±0.04)	
	80	0.72	0.07	0.01	0.20	0.00			0.80 (±0.04)	
Na/Sr	Room	0.88	0.06	0.01	0.03	0.02				0.84 (±0.04)
	80	0.86	0.06	0.01	0.05	0.02				0.85 (±0.04)
Na/(K,Ca,Mg,Sr)	Room	0.37	0.07	0.37	0.17	0.02	1.11 (±0.03)	0.74 (±0.04)	0.71 (±0.02)	0.86 (±0.02)
	80	0.38	0.06	0.36	0.18	0.02	1.00 (±0.03)	0.77 (±0.03)	0.80 (±0.03)	0.95 (±0.02)
Na/(K,Ca,Mg,Sr)*	25	0.17	0.04	0.45	0.33	0.01	1.04	0.94	0.85	1.02
Model at 25 °C*	25						1.2	0.7	0.7	0.6

* From Gaucher et al. (2009).

position such as Fe-rich calcite, Fe-rich dolomite, ankerite, sideroplesite, or siderite (Tournassat et al., 2008; Lerouge et al., 2011, 2013). This makes it difficult to quantify dissolution of half of the stock of the Fe-carbonate minerals. Our Mössbauer spectrometry results showed that the proportion of iron associated with carbonate minerals did not change significantly during the hydrothermal alteration of the sample, but our magnetic remanence measurements evinced the precipitation of siderite with temperature. The combination of these two results indicates that dissolution and re-precipitation of Fe in carbonate minerals compensated each other over the course of the experiment. Similarly, the variations in the amount of dolomite that may have occurred during the experiment are difficult to estimate from XRD patterns, because of the low dolomite content (Fig. 3), of its heterogeneous chemical composition, and of the refinement code we used. Although chlorite particles could be unambiguously detected in the clay-rock (Gaucher et al., 2004; Grangeon et al., 2015), the exact amount of chlorite was also very difficult to quantify for the same reason as for dolomite. In these conditions, even a 100 % increase in chlorite content might have been difficult to measure. Chlorite minerals in the Callovian-Oxfordian formation are Fe-rich chlorites and similar in composition to the Chlorite-Cca2/Ripidolite-Cca2 in the thermodynamic databases (Lerouge et al., 2011). In our experiments, the increased contribution of Fe associated with clay minerals could therefore be the only indirect evidence of chlorite precipitation. However, precipitation of Fe in, or adsorption of Fe on the surface of other clay minerals could also explain this observation. Because Fe in clay layers are known to be redox reactive (Gorski et al., 2013; Hadi et al., 2013; Sander et al., 2015), we cannot rule out the redox state of structural Fe in the clay layers a changing with temperature either.

This analysis highlights the fact that only neo-formed phases, i.e. the phases that were not present in the initial mineralogical assemblage, could be unambiguously interpreted as a consequence of the hydrothermal alteration. In our experiments, we could detect only two of them: anhydrite and acicular goethite. The presence of anhydrite in samples reacted at 80 °C was not surprising because the initial solutions (and the pore water in the clay-rock as well) were only slightly undersaturated with gypsum. The model should thus include the possible precipitation of this phase. In our opinion, the presence of goethite in reacted samples could not be attributed to the oxidation of the sample by atmospheric O_2 during the experiment: first, the measured p_{O2} remained below the detection limit for experiments 1 and 2; second, the degradation of the cobaltihexammine molecule during the cation exchange experiment was indicative that the sample's redox properties were well preserved (Hadi et al., 2016); and third, the presence of acicular goethite in reacted samples is in agreement with the recent finding that nanocrystalline goethite is present in pristine Callovian-Oxfordian and Opalinus Clay samples (Kars et al., 2015). The co-existence of goethite and pyrite in a supposedly reduced environment might be surprising at first sight, but is possible on a thermodynamics point of view. Indeed, the consideration of goethite in a

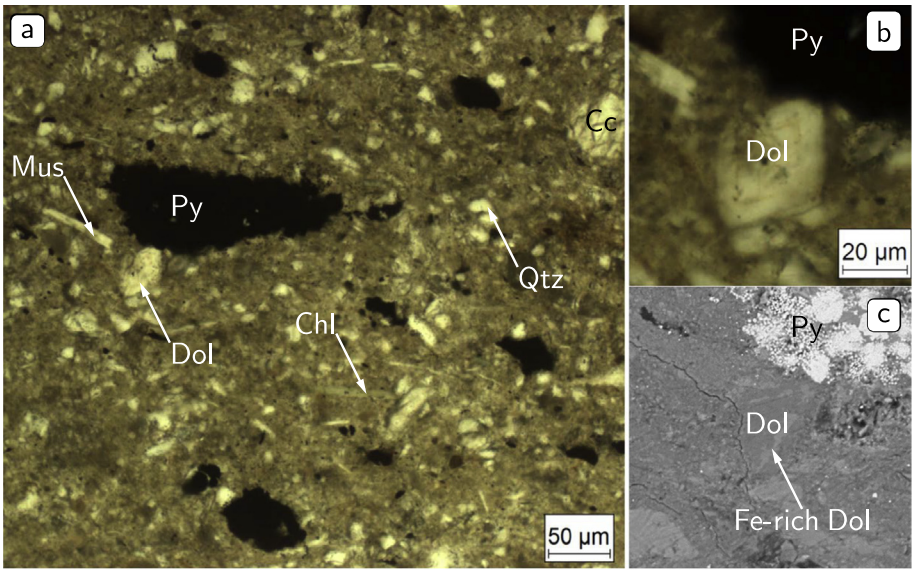

Fig. 11. (a) General texture and mineralogy of the initial sample showing euhedral grains of calcite and dolomite in the clay-rock (natural transmitted light); (b) detail of the rhombohedral dolomite grain (natural transmitted light); (c) Backscattered electron image of the rhombohedral dolomite grain providing evidence of slight iron-enrichment of its rims.

Table 6
Mineralogical assemblage considered for modeling the hydrothermal experiments. The relative phase abundances were taken from Marty et al. (2015), and they were converted into mol·L^{-1} with the solid/liquid ratio used in our experiments (100 g·L^{-1}). N.A. = Not applicable.

Mineral name	Initial amount (model estimation) (mol·L^{-1})	Modeled variations after equilibrium at 80 °C	
		Modeled variation Fast reacting system (%)	Modeled variation Whole system (%)
Calcite	0.232	−1	+3
Celestite	0.006	−7	−7
Dolomite	0.023	+5	−36
Siderite	0.009	−1	−50
Chlorite-Cca2/Ripidolite-Cca2	0.003	N.A.	+100
Illite-IMt2	0.089	N.A.	−4
Pyrite	0.009	N.A.	−0.3
Quartz	0.421	N.A.	+1

model of pore water composition at 25 °C made it possible already to reconcile the model results with the Fe concentrations measured in seepage water samples from *in situ* instrumented boreholes (Kars et al., 2015; Tournassat et al., 2015). Although it is not possible to discard completely the possibility of a limited sample oxidation by O_2, all the possible precautions were taken to avoid it, and we believe that goethite should be considered in the pore water equilibrium model at 80 °C for a pristine sample.

4.2. Model enhancement

We recall that any change in the pore water model must respect the constraints of the Gibbs' phase rule explained in the Materials and Method section. In particular, it is not possible to increase the number of phases to a value greater than the number of independent components. The addition of the possible precipitation of anhydrite in the pore water model at 80 °C was not problematic because the sulfate/Ca/Sr subsystem can accommodate an additional phase that modifies the cation exchange composition in turn (Tournassat et al., 2015). The addition of goethite was more problematic since goethite competes directly with the presence of siderite in the model. Since there was some experimental evidence that Fe-carbonate minerals were reactive, but that their nature changed with temperature, we decided to replace siderite by goethite. This choice was also in agreement with our last version of the pore water model at 25 °C (Kars et al., 2015; Tournassat et al., 2015). The total concentration of goethite was set at a very low value ($7 \cdot 10^{-4}$ mol·L^{-1}), which corresponded roughly to the amount of goethite in the sample as estimated from magnetic remanence measurements.

Speciation calculations made with the measured concentrations and the Thermochimie database (Giffaut et al., 2014) predicted undersaturation of anhydrite in all of the

Table 7
Comparison of 80 °C clay-rock/water interaction models with concentrations measured in experiment 2 and observations made on the solids at the end of the hydrothermal alteration experiments. Calculations used the Thermoddem database.

Components	Measurements in Exp. 2	Models			
		Predictive model "whole system"	+goethite +anhydrite −siderite	+goethite + anhydrite −siderite −chlorite	+goethite +anhydrite −chlorite 0.0023 mmol·L^{-1} of siderite
Solution					
pH	6.6	6.0	6.5	6.7	6.4
$\log_{10} p_{CO2}$	−1.1	−0.39	−1.3	−1.6	−1.1
mmol·L^{-1}					
Ca	8.8	13	11	11	11
Mg	3.2	3.6	3.2	3.1	3.2
Na	41	46	46	46	46
K	1.6	4.0	2.3	2.0	2.1
Cl	44	44	44	44	44
Sulfate	10	11	9.3	9.3	9.2
Sr	0.12	0.20	0.21	0.20	0.21
DIC	1.1	9.1	2.2	1.2	2.7
Alkalinity	1.3	3.9	1.5	1.0	1.8
Fe	$5.7 \cdot 10^{-3}$	$100 \cdot 10^{-3}$	$0.43 \cdot 10^{-3}$	$4.5 \cdot 10^{-3}$	$13 \cdot 10^{-3}$
Al	$3.2 \cdot 10^{-4}$	$2.8 \cdot 10^{-4}$	$8.6 \cdot 10^{-4}$	$5.6 \cdot 10^{-4}$	$4.7 \cdot 10^{-4}$
Si	0.59	0.70	0.70	0.70	0.70
Exchanger					
E_{Na}	0.10*	0.18	0.20	0.20	0.20
E_K	0.08	0.15	0.10	0.09	0.08
E_{Ca}	0.67**	0.51	0.54	0.55	0.55
E_{Mg}	0.12	0.15	0.16	0.16	0.16
E_{Sr}	0.03***	0.006	0.007	0.008	0.008
Solid					
Anhydrite	Precipitation	Not considered	Precipitation (1.8 mmol·L^{-1})	Precipitation (1.7 mmol·L^{-1})	Precipitation (1.5 mmol·L^{-1})
Goethite	Re-precipitation of needle-shaped particles	Not considered	Complete dissolution	Limited dissolution ($9.4 \cdot 10^{-4}$ mmol·L^{-1})	Precipitation (2.2 mmol·L^{-1})
Siderite/Fe-carbonate	Limited reactivity Re-precipitation	−60 % dissolution	Not considered (SI = −2.3)	Not considered (SI = −1.5)	Complete dissolution of available Fe carbonate (SI = −0.7)
Chlorite/Fe-bearing clay	No convincing experimental evidence	+100 % precipitation	Limited precipitation (+2 %)	Not considered (SI = +3.0)	Not considered (SI = + 1.7)

* This value has the largest uncertainty due to the background correction.
** This value may include a contribution from gypsum and calcite dissolution during the exchange experiment procedure (Dohrmann and Kaufhold, 2009; Gaucher et al., 2009).
*** This value may include a contribution from celestite dissolution during the exchange experiment procedure (Gaucher et al., 2009).

experiments in contradiction with the observation of anhydrite precipitation. Since the Thermoddem database (Blanc et al., 2012) correctly predicted the saturation or an oversaturation of anhydrite in the same conditions, we used this database for the following calculations.

Using the goethite + anhydrite model without consideration of siderite we reproduced the data from experiment 2 quite accurately (5th column in Table 7). In particular, the model predicted a correct pH value and anhydrite precipitation. However, some results of the model were not in agreement with observations: the p_{CO2} was too low ($10^{-1.6}$ bar instead of $10^{-1.1}$ bar) and complete dissolution of goethite was predicted instead of the observed precipitation. In this simulation, limited chlorite precipitation was also predicted and its precipitation consumed the iron that was made available through goethite dissolution. According to Mosser-Ruck et al. (2010), the precipitation of chlorite is favored at temperatures over 150 °C. Therefore, chlorite precipitation should be perhaps neglected in our experimental conditions (twenty months at 80 °C). The removal of chlorite in the model inhibited the dissolution of goethite (but still no precipitation was predicted), and led to a predicted Fe concentration in solution in agreement with what was measured (6th column in Table 7). It was surprising, at first sight, to see how the Fe system impacted the pH and the p_{CO2} values at 80 °C. At 25 °C, it was demonstrated that the Fe subsystem had little influence on pH or p_{CO2} (Gaucher et al., 2009). However at 80 °C, in the presence of siderite, the model predicted a log p_{CO2} value of −0.39 while, in the absence of siderite this value dropped to −1.6. Consequently, we decided to test the effect of limited siderite dissolution (or Fe-bearing carbonate) on the outcome of the simulation. By adjusting the amount of available siderite to 0.0023 mmol·L^{-1}, it was possible to accurately reproduce all of the measured concentrations and the observations made on the solid phase. The dissolved inorganic carbon (DIC) concentration was the only values that was strongly overestimated (Table 7). However, we should note that the measured pH, p_{CO2}, DIC and alkalinity values were not fully mutually consistent in our experiments. The DIC measurement is especially sensitive to degassing while the alkalinity value is conservative in the presence of degassing. Since the pH and p_{CO2} values were measured online, the DIC value was the most prone to experimental degassing artifacts. The DIC value predicted by the model was higher than the measured value, in agreement with our interpretation.

4.3. 80 °C pore water composition models

The model enhancement given above was not entirely satisfying: as such, the model could not be considered to be predictive because a fitted parameter (the amount of reactive Fe-carbonate minerals) was necessary to reproduce our experimental data. Consequently, we decided to test the model on the independent dataset from Beaucaire et al. (2012). The experiments from Beaucaire et al. (2012) were carried out with a solid to liquid ratio (1.3 kg·L^{-1}) that was ten times higher than ours and with an initial p_{CO2} of 0.4 bar in the gas phase of their autoclave. Since these experimental conditions were very different from ours, we considered that our model successfully predicting their data would be convincing evidence of our model's reliability. For our modeling test, we kept the same proportion of reacting Fe-carbonate as in the model described in the previous paragraph. The results of our model compared very well with this independent set of experimental data (Table 8). In particular, our model predicted increased p_{CO2} even in the presence of a rather large value for initial p_{CO2}. This result evinced the fact that the solution composition prediction was dependent on the solid to liquid ratio and on the initial p_{CO2} of the experiment. Contrary to the models developed at 25 °C where a fixed composition of the cation exchanger and a mineralogical assemblage made

Table 8
Comparison of our 80 °C clay-rock/water interaction models with the experimental data from Beaucaire et al. (2012) (15 months, 80 °C). n.p. = not provided; n.m. = not measured. Calculations were made with the Thermoddem database.

Components	Measurements		Models		
	Initial solution	Final solution	Model from Beaucaire et al. (2012)	Our model	Our model + oxidation
Solution					
pH	6.16	n.p.	6.16	6.0	5.9
$\log_{10} p_{CO2}$	−0.40	0.04	−0.36	−0.18	0.04
mmol·L^{-1}					
Ca	7.0	6.9	7.2	7.5	9.6
Mg	1.9	2.6	1.7	2.2	2.8
Na	51	51	48	50	53
K	0.95	2.3	0.9	1.5	1.6
Cl	49	58	50	49	49
Sulfate	7.5	6.6	6.7	8.2	12
Sr	n.m.	0.10	0.22	0.24	0.20
DIC	n.p.	n.p.	4.9*	14	21
Alkalinity	5.1	7.9	n.p.	6.1	7.3
Fe	n.p.	n.p.	$57 \cdot 10^{-3}$	$62 \cdot 10^{-3}$	$80 \cdot 10^{-3}$
Al	n.p.	$3.7 \cdot 10^{-4}$	$1.8 \cdot 10^{-4}$	$4.7 \cdot 10^{-4}$	$4.8 \cdot 10^{-4}$
Si	n.p.	0.56	0.62	0.70	0.70

Table 9
Comparison of predictive models for pore water composition at 80 °C and at otherwise *in situ* conditions in the Callovian-Oxfordian Formation. n.p. = not provided.

Components	Beaucaire et al. (2012)	Our initial model* (Thermochimie)	Our initial model* (Thermoddem)	Our final model
pH	6.16	6.0	6.0	6.0
$\log_{10} p_{CO2}$	−0.36	−0.29	−0.24	−0.15
Ca	7.2	12	10	9.9
Mg	1.7	3.4	2.8	2.9
Na	48	43	40	39
K	0.9	1.0	0.99	0.96
Cl	50	41	41	41
Sulfate	6.7	15	11	10
Sr	0.22	0.26	0.19	0.21
DIC	4.9**	11	12	14
Alkalinity	n.p.	5.7	5.0	5.6
Fe	$57{\cdot}10^{-3}$	$68 \cdot 10^{-3}$	$86 \cdot 10^{-3}$	$82 \cdot 10^{-3}$
Al	$1.8{\cdot}10^{-4}$	$5.8 \cdot 10^{-4}$	$5.1 \cdot 10^{-4}$	$5.3 \cdot 10^{-4}$
Si	0.62	0.69	0.70	0.70

* Complete mineralogical assemblage.
** This value reported as a DIC value in Beaucaire et al. (2012) corresponds in fact to an alkalinity value.

it possible to reach the constraint $F = 0$ (or alternatively $C = P$, see Eq. (1) and the Gibbs' phase rule), the model at 80 °C lets the cation exchanger composition readjust as the temperature increases. This way, the cation exchanger cannot be considered to be a constraint in the sense of the Gibbs' phase rule anymore (Tournassat et al., 2015). This was also true for the model of Beaucaire et al. (2012) whose discrepancy with the measured p_{CO2} ($10^{-0.36}$ bar versus $10^{0.04}$ bar) was attributed by these authors to the uncertainty on the solubility constants of clay minerals (kaolinite and chlorite). The possible effect of O_2 intrusion in the autoclave, which was indeed documented in their study with pO_2 as high as 0.03 % at the end of their experiment, and the subsequent decrease of pH due to the oxidation of pyrite was discarded by the authors because the sulfate concentration did not increase during their experiment. Their first explanation cannot be ruled out. The effect of the uncertainty of the clay mineral solubility constant had already been thoroughly examined for clay-rocks' pore water composition at 25 °C (Gaucher et al., 2009; Pearson et al., 2011), and the conclusions were similar to those of Beaucaire et al. (2012). However, the effect of O_2 intrusion cannot be ruled out too. Our model predicted that the intrusion of a total (fitted) amount of 0.072 mol of O_2 in their autoclave could have led to the observed p_{CO2} increase (Table 8) without dramatically changing the solution composition (6th column in Table 8). Interestingly, the precipitation of goethite was not predicted by our model in the experimental conditions of Beaucaire et al. (2012), which could explain why they did not report its presence in their reacted samples.

Since the results of the models at 80 °C depended on the solid to liquid ratio considered, we recalculated the expected pore water composition at *in situ* condition by considering a solid to liquid ratio of 55.5 corresponding to a sample density of 2.2 $kg{\cdot}dm^{-3}$ and a free pore water content of 0.04 $kg_{water}{\cdot}kg_{rock}^{-1}$. The results are reported in Table 9 together with the results of our *a priori* predictive model and this of Beaucaire et al. (2012). Despite their differences in concept, modeling hypotheses and database, all of the reported models predicted very similar pore water compositions.

5. SUMMARY AND CONCLUSION

The similarity between the pore water composition predictions made with the various models described in this study is a blatant demonstration that the results of hydrothermal experiments with clay-rocks cannot demonstrate the validity of a thermodynamic equilibrium model at 80 °C in these systems. Two main reasons explain this failure. The first is that the models at 80 °C are not fully constrained in the sense of the Gibbs' phase rule because the exchanger composition cannot be fixed at measured values as it is the case for models at 25 °C. The second reason is linked to the fact that, contrary to the models developed at 25 °C, models at 80 °C are not constrained easily by analyzing solid samples having reacted at 80 °C, even for a long time. Thermodynamic equilibria cannot be assessed in these experiments and most predicted mineralogy changes are so subtle, compared to the inherent complexity of the clay-rock composition and of its characterization, that tracking these changes can be compared to finding a needle in a haystack. The only unambiguous mineralogical constraints that we could find in our experiments were the neoformation of goethite and anhydrite. These observations made it possible to assess the prominent role of Fe-bearing phases in the outcome of the experiments, especially for the measured pH and p_{CO2} values. After calibrating the amount of reacting Fe-bearing carbonate phases with our data, we showed that the proposed model was also capable of predicting the chemical evolution of another system published in the literature, which used the same clay-rock material but with significant differences in experimental conditions (especially higher initial p_{CO2} and solid to liquid ratio). This result gave confidence in the

model predictions but was not deemed sufficient to be confident in the model adequacy and usefulness in conditions different than the one experimentally tested. To predict pore water chemistry as a function of temperature, we need a better understanding of the equilibria taking place in the Fe–Ca–Mg carbonate system as a function of temperature. In addition, explicit consideration of kinetics in the models may be necessary to assess whether a thermodynamic equilibrium can be attained in the time frame of an *in situ* thermal perturbation. To take steps to achieve this, we have launched ten-year equilibration experiments.

ACKNOWLEDGEMENTS

The results presented in this article were collected during the THERMOAR and CTEC Projects granted by Andra in the framework of the Andra/BRGM scientific partnership. We thank V. Laperche and N. Maubec (BRGM) for their help with the solid samples analysis.

REFERENCES

Altmann S. (2008) Geo'chemical research: a key building block for nuclear waste disposal safety cases. *J. Contam. Hydrol.* **102**, 174–179.

Andra, 2005. Référentiel du comportement des radionucléides et des toxiques chimiques d'un stockage dans le Callovo-Oxfordien jusqu'à l'Homme. Dossier 2005 Argile. Agence Nationale pour la gestion des déchets radioactifs, Châtenay-Malabry, France.

Beaucaire C., Pitsch H., Toulhoat P., Motellier S. and Louvat D. (2000) Regional fluid characterisation and modelling of water-rock equilibria in the Boom Clay Formation and in the Rupelian aquifer at Mol, Belgium. *Appl. Geochem.* **15**, 667–686.

Beaucaire C., Michelot J. L., Savoye S. and Cabrera J. (2008) Groundwater characterisation and modelling of water-rock interaction in an argillaceous formation (Tournemire, France). *Appl. Geochem.* **23**, 2182–2197.

Beaucaire C., Tertre E., Ferrage E., Grenut B., Pronier S. and Madé B. (2012) A thermodynamic model for the prediction of pore water composition of clayey rock at 25 and 80 °C – comparison with results from hydrothermal alteration experiments. *Chem. Geol.* **334**, 62–76.

Bianchi M., Liu H.-H. and Birkholzer J. T. (2014) Radionuclide transport behavior in a generic geological radioactive waste repository. *Groundwater* **53**, 440–451.

Blanc P., Lassin A., Piantone P., Azaroual M., Jacquemet N., Fabbri A. and Gaucher E. C. (2012) Thermoddem: A geochemical database focused on low temperature water/rock interactions and waste materials. *Appl. Geochem.* **27**, 2107–2116.

Bradbury M. H. and Baeyens B. (1998) A physicochemical characterisation and geochemical modelling approach for determining porewater chemistries in argillaceous rocks. *Geochim. Cosmochim. Acta* **62**, 783–795.

Cama J., Ganor J., Ayora C. and Lasaga C. A. (2000) Smectite dissolution kinetics at 80 °C and pH 8.8. *Geochim. Cosmochim. Acta* **64**, 2701–2717.

Chichagov A. V. (1994) Information-calculating system on crystal structure data of minerals (MINCRYST). In *Materials Science Forum*. Trans Tech Publ, pp. 193–198.

Claret F., Sakharov B. A., Drits V. A., Velde B., Meunier A., Griffault L. and Lanson B. (2004) Clay minerals in the Meuse-Haute Marne underground laboratory (France): Possible influence of organic matter on clay mineral evolution. *Clays Clay Miner.* **52**, 515–532.

Claret F., Lerouge C., Laurioux T., Bizi M., Conte T., Ghestem J. P., Wille G., Sato T., Gaucher E. C., Giffaut E. and Tournassat C. (2010) Natural iodine in a clay formation: Implications for iodine fate in geological disposals. *Geochim. Cosmochim. Acta* **74**, 16–29.

Danzer K. (2007) *Analytical Chemistry. Theoretical and Metrological Fundamentals*. Springer, Heidelberg.

Dekkers M. J. (1989) Magnetic properties of natural goethite—II. TRM behaviour during thermal and alternating field demagnetization and low-temperature treatment. *Geophys. J. Int.* **97**, 341–355.

Delay J., Vinsot A., Krieguer J.-M., Rebours H. and Armand G. (2007) Making of the underground scientific experimental programme at the Meuse/Haute-Marne underground research laboratory, North Eastern France. *Phys. Chem. Earth Parts A/B/C* **32**, 2–18.

Didier M., Géhin A., Grenèche J.-M., Charlet L. and Giffaut E. (2014) Method development for evaluating the redox state of Callovo-Oxfordian clayrock and synthetic montmorillonite for nuclear waste management. *Appl. Geochem.* **49**, 184–191.

Dohrmann R. and Kaufhold S. (2009) Three new, quick CEC methods for determining the amounts of exchangeable calcium cations in calcareous clays. *Clays Clay Miner.* **57**, 338–352.

Fernández A. M., Sánchez-Ledesma D. M., Tournassat C., Melón A., Gaucher E. C., Astudillo J. and Vinsot A. (2014) Applying the squeezing technique to highly Consolidated clayrocks for pore water characterisation: Lessons learned from experiments at the Mont Terri Rock Laboratory. *Appl. Geochem.* **49**, 2–21.

Frederichs T., Von Dobeneck T., Bleil U. and Dekkers M. J. (2003) Towards the identification of siderite, rhodochrosite, and vivianite in sediments by their low-temperature magnetic properties. *Phys. Chem. Earth Parts A/B/C* **28**, 669–679.

Gaboreau S., Claret F., Crouzet C., Giffaut E. and Tournassat C. (2012) Caesium uptake by Callovian-Oxfordian clayrock under alkaline perturbation. *Appl. Geochem.* **27**, 1194–1201.

Gaines G. L. J. and Thomas H. C. (1953) Adsorption studies on clay minerals. II. A formulation of the thermodynamics of exchange adsorption. *J. Chem. Phys.* **21**, 714–718.

Gaucher E. C. and Blanc P. (2006) Cement/clay interactions - A review: Experiments, natural analogues, and modeling. *Waste Manage.* **26**, 776–788.

Gaucher E., Robelin C., Matray J.-M., Negrel G., Gros Y., Heitz J. F., Vinsot A., Rebours H., Cassabagnere A. and Bouchet A. (2004) ANDRA underground research laboratory: Interpretation of the mineralogical and geochemical data acquired in the Callovian-Oxfordian Formation by investigative drilling. *Phys. Chem. Earth Parts A/B/C* **29**, 55–77.

Gaucher E. C., Blanc P., Bardot F., Braibant G., Buschaert S., Crouzet C., Gautier A., Girard J.-P., Jacquot E., Lassin A., Negrel G., Tournassat C., Vinsot A. and Altmann S. (2006) Modelling the porewater chemistry of the Callovian-Oxfordian Formation at a regional scale. *C.R. Geosci.* **338**, 917–930.

Gaucher E. C., Tournassat C., Pearson F. J., Blanc P., Crouzet C., Lerouge C. and Altmann S. (2009) A robust model for pore-water chemistry of clayrock. *Geochim. Cosmochim. Acta* **73**, 6470–6487.

Giffaut E., Grivé M., Blanc P., Vieillard P., Colàs E., Gailhanou H., Gaboreau S., Marty N., Madé B. and Duro L. (2014) Andra thermodynamic database for performance assessment: ThermoChimie. *Appl. Geochem.* **49**, 225–236.

Gorski C. A., Klüpfel L. E., Voegelin A., Sander M. and Hofstetter T. B. (2013) Redox properties of structural Fe in clay minerals: 3. Relationships between smectite redox and structural properties. *Environ. Sci. Technol.* **47**, 13477–13485.

Grangeon S., Vinsot A., Tournassat C., Lerouge C., Giffaut E., Heck S., Groschopf N., Denecke M. A., Wechner S. and Schäfer T. (2015) The influence of natural trace element distribution on the mobility of radionuclides. The exemple of nickel in a clay-rock. *Appl. Geochem.* **52**, 155–173.

Guyodo Y., LaPara T. M., Anschutz A. J., Penn R. L., Banerjee S. K., Geiss C. E. and Zanner W. (2006) Rock magnetic, chemical and bacterial community analysis of a modern soil from Nebraska. *Earth Planet. Sci. Lett.* **251**, 168–178.

Hadi J., Tournassat C., Ignatiadis I., Greneche J.-M. and Charlet L. (2013) Modelling CEC variations versus structural iron reduction levels in dioctahedral smectites. Existing approaches, new data and model refinements. *J. Colloid Interface Sci.* **407**, 397–409.

Hadi J., Tournassat C. and Lerouge C. (2016) Pitfalls in using the hexammine cobalt method for cation exchange capacity measurements on clay minerals and clay-rocks: redox interferences between the cationic dye and the sample. *Appl. Clay Sci.* **119**, 339–400.

Housen B. A., Banerjee S. and Moskowitz B. (1996) Low temperature magnetic properties of siderite and magnetite in marine sediments. *Geophys. Res. Lett.* **23**, 2843.

Kars M., Lerouge C., Grangeon S., Aubourg C., Tournassat C., Madé B. and Claret F. (2015) Identification of nanocrystalline goethite in reduced clay formations. Application to the Callovian-Oxfordian formation of Bure (France). *Am. Mineral.* **100**, 1544–1553.

Landais P. (2006) Advances in geochemical research for the underground disposal of high-level, long-lived radioactive waste in a clay formation. *J. Geochem. Explor.* **88**, 32–36.

Lerouge C., Grangeon S., Gaucher E. C., Tournassat C., Agrinier P., Guerrot C., Widory D., Flehoc C., Wille G., Ramboz C., Vinsot A. and Buschaert S. (2011) Mineralogical and isotopic record of biotic and abiotic diagenesis of the Callovian-Oxfordian clayey formation of Bure (France). *Geochim. Cosmochim. Acta* **75**, 2633–2663.

Lerouge C., Vinsot A., Grangeon S., Wille G., Fléhoc C., Gailhanou H., Gaucher E. C., Madé B., Altmann S. and Tournassat C. (2013) Controls of Ca/Mg/Fe activity ratios in pore water chemistry models of the Callovian-Oxfordian clay formation. *Proc. Earth Planet. Sci.* **7**, 475–478.

Marty N. C. M., Tournassat C., Burnol A., Giffaut E. and Gaucher E. C. (2009) Influence of reaction kinetics and mesh refinement on the numerical modelling of concrete/clay interactions. *J. Hydrol.* **364**, 58–72.

Marty N. C. M., Cama J., Sato T., Chino D., Villiéras F., Razafitianamaharavo A., Brendlé J., Giffaut E., Soler J. M., Gaucher E. C. and Tournassat C. (2011) Dissolution kinetics of synthetic Na-smectite. An integrated experimental approach. *Geochim. Cosmochim. Acta* **75**, 5849–5864.

Marty N. C. M., Munier I., Gaucher E. C., Tournassat C., Gaboreau S., Vong Chan Q., Giffaut E., Cochepin B. and Claret F. (2014) Simulation of cement/clay interactions: feedback on the increasing complexity of modelling strategies. *Transp. Porous Media* **104**, 385–405.

Marty N. C. M., Claret F., Lassin A., Tremosa J., Blanc P., Madé B., Giffaut E., Cochepin B. and Tournassat C. (2015) A database of dissolution and precipitation rates for clay-rocks minerals. *Appl. Geochem.* **55**, 108–118.

Mazurek M., Oyama T., Wersin P. and Alt-Epping P. (2015) Porewater squeezing from indurated shales. *Chem. Geol.* **400**, 106–121.

Moore R. (1991) The chemical and mineralogical controls upon the residual strength of pure and natural clays. *Geotechnique* **41**, 35–47.

Mosser-Ruck R., Cathelineau M., Guillaume D., Charpentier D., Rousset D., Barres O. and Michau N. (2010) Effects of temperature, pH, and iron/clay and liquid/clay ratios on experimental conversion of dioctahedral smectite to berthierine, chlorite, vermiculite, or saponite. *Clays Clay Miner.* **58**, 280–291.

Motellier S., Ly J., Gorgeon L., Charles Y., Hainos D., Meier P. and Page J. (2003) Modelling of the ion-exchange properties and indirect determination of the interstitial water composition of an argillaceous rock. Application to the Callovo-Oxfordian low-water-content formation. *Appl. Geochem.* **18**, 1517–1530.

Muxworthy A. and McClelland E. (2000) Review of the low-temperature magnetic properties of magnetite from a rock magnetic perspective. *Geophys. J. Int.* **140**, 101–114.

Neuzil C. E. (2013) Can shale safely host US nuclear waste? *Eos Trans. Am. Geophys. Union* **94**, 261–262.

Özdemir O. and Dunlop D. J. (1996) Thermoremanence and Néel temperature of goethite. *Geophys. Res. Lett.* **23**, 921–924.

Özdemir Ö., Dunlop D. J. and Moskowitz B. M. (2002) Changes in remanence, coercivity and domain state at low temperature in magnetite. *Earth Planet. Sci. Lett.* **194**, 343–358.

Parkhurst, D.L., Appelo, C.A.J., 1999. User's guide to PHREEQC (Version 2) – A computer program for speciation, batch-reaction, one-dimensional transport, and inverse geochemical calculations. Denver, CO. U.S. Geological Survey. Water resources investigations report 99–4259, pp. 312.

Parkhurst, D.L., Appelo, C.A.J., 2013. Description of input and examples for PHREEQC Version 3– a computer program for speciation, batch-reaction, one-dimensional transport, and inverse geochemical calculations. U.S. Geological Survey Techniques and Methods, book 6, chap. A43, 497 p., available at <http://pubs.usgs.gov/tm/06/a43/>.

Pearson, F.J., Arcos, D., Boisson, J.-Y., Fernandez, A.-M., Gäbler, H.-E., Gaucher, E., Gautschi, A., Griffault, L., Hernan, P., Waber, H.N., 2003. Mont Terri project – Geochemistry of water in the Opalinus clay formation at the Mont Terri Rock Laboratory. Geology Series No. 5 Swiss Federal Office for Water and Geology, Bern.

Pearson F. J., Tournassat C. and Gaucher E. C. (2011) Biogeochemical processes in a clay formation in situ experiment: Part E - Equilibrium controls on chemistry of pore water from the Opalinus Clay, Mont Terri Underground Research Laboratory, Switzerland. *Appl. Geochem.* **26**, 990–1008.

Rosenqvist I. T. (1984) The importance of pore water chemistry on mechanical and engineering properties of clay soils. *Philos. Trans. R. Soc. Lond. Ser. A* **311**, 369–373.

Rozalén M. L., Huertas F. J., Brady P. V., Cama J., García-Palma S. and Linares J. (2008) Experimental study of the effect of pH on the kinetics of montmorillonite dissolution at 25 & #xB0;C. *Geochim. Cosmochim. Acta* **72**, 4224–4253.

Rozalén M., Brady P. V. and Huertas F. J. (2009) Surface chemistry of K-montmorillonite: Ionic strength, temperature dependence and dissolution kinetics. *J. Colloid Interface Sci.* **333**, 474–484.

Sander M., Hofstetter T. B. and Gorski C. A. (2015) Electrochemical analyses of redox-active iron minerals: a review of nonmediated and mediated approaches. *Environ. Sci. Technol.* **49**, 5862–5878.

Savage D., Noy D. and Mihara M. (2002) Modelling the interaction of bentonite with hyperalkaline fluids. *Appl. Geochem.* **17**, 207–223.

Tournassat C., Gailhanou H., Crouzet C., Braibant G., Gautier A., Lassin A., Blanc P. and Gaucher E. C. (2007) Two cation exchange models for direct and inverse modelling of solution major cation composition in equilibrium with illite surfaces. *Geochim. Cosmochim. Acta* **71**, 1098–1114.

Tournassat C., Lerouge C., Blanc P., Brendle J., Greneche J.-M., Touzelet S. and Gaucher E. C. (2008) Cation exchanged Fe(II) and Sr compared to other divalent cations (Ca, Mg) in the Bure Callovian-Oxfordian Formation: Implications for porewater composition modelling. *Appl. Geochem.* **23**, 641–654.

Tournassat C., Gailhanou H., Crouzet C., Braibant G., Gautier A. and Gaucher E. C. (2009) Cation exchange selectivity coefficient values on smectite and mixed-layer illite/smectite minerals. *Soil Sci. Soc. Am. J.* **73**, 928–942.

Tournassat C., Vinsot A., Gaucher E. C. and Altmann S. (2015) Chapter 3 – Chemical conditions in clay-rocks. In *Natural and Engineered Clay Barriers, Developments in Clay Science* (eds. C. Tournassat, C. I. Steefel, I. C. Bourg and F. Bergaya). Elsevier, pp. 71–100.

Tremosa J., Arcos D., Matray J.-M., Bensenouci F., Gaucher E. C., Tournassat C. and Hadi J. (2012) Geochemical characterization and modelling of the Toarcian/Domerian porewater at the Tournemire underground research laboratory. *Appl. Geochem.* **27**, 1417–1431.

Vinsot A., Mettler S. and Wechner S. (2008) In situ characterization of the Callovo-Oxfordian pore water composition. *Phys. Chem. Earth Parts A/B/C* **33**, S75–S86.

Zachara J., Brantley S., Chorover J., Ewing R., Kerisit S., Liu C., Perfect E., Rother G. and Stack A. G. (2016) Internal domains of natural porous media revealed: critical locations for transport, storage, and chemical reaction. *Environ. Sci. Technol.* **50**, 2811–2829.

Associate editor: Annie B. Kersting